

# Influences of Environmental Relative Humidity and Horizontal Scale of Subcloud Ascent on Deep Convective Initiation

HUGH MORRISON,<sup>a,b</sup> JOHN M. PETERS,<sup>c</sup> KAMAL KANT CHANDRAKAR,<sup>a</sup> AND STEVEN C. SHERWOOD<sup>b</sup>

<sup>a</sup> National Center for Atmospheric Research, Boulder, Colorado

<sup>b</sup> Climate Change Research Centre, ARC Centre of Excellence for Climate Extremes, University of New South Wales, Sydney, Australia

<sup>c</sup> Department of Meteorology, Naval Postgraduate School, Monterey, California

(Manuscript received 1 March 2021, in final form 28 July 2021)

**ABSTRACT:** This study examines two factors impacting initiation of moist deep convection: free-tropospheric environmental relative humidity ( $\phi_E$ ) and horizontal scale of subcloud ascent ( $R_{\text{sub}}$ ), the latter exerting a dominant control on cumulus cloud width. A simple theoretical model is used to formulate a “scale selection” hypothesis: that a minimum  $R_{\text{sub}}$  is required for moist convection to go deep, and that this minimum scale decreases with increasing  $\phi_E$ . Specifically, the ratio of  $R_{\text{sub}}^2$  to saturation deficit ( $1 - \phi_E$ ) must exceed a certain threshold value that depends on cloud-layer environmental lapse rate. Idealized, large-eddy simulations of moist convection forced by horizontally varying surface fluxes show strong sensitivity of maximum cumulus height to both  $\phi_E$  and  $R_{\text{sub}}$  consistent with the hypothesis. Increasing  $R_{\text{sub}}$  by only 300–400 m can lead to a large increase ( $>5$  km) in cloud height. A passive tracer analysis shows that the bulk fractional entrainment rate decreases rapidly with  $R_{\text{sub}}$  but depends little on  $\phi_E$ . However, buoyancy dilution increases as either  $R_{\text{sub}}$  or  $\phi_E$  decreases; buoyancy above the level of free convection is rapidly depleted in dry environments when  $R_{\text{sub}}$  is small. While deep convective initiation occurs with an increase in relative humidity of the near environment from moistening by earlier convection, the importance of this moisture preconditioning is inconclusive as it is accompanied by an increase in  $R_{\text{sub}}$ . Overall, it is concluded that small changes to  $R_{\text{sub}}$  driven by external forcing or by convection itself could be a dominant regulator of deep convective initiation.

**KEYWORDS:** Entrainment; Buoyancy; Convective-scale processes; Cumulus clouds; Large eddy simulations

## 1. Introduction

A thermodynamic profile with convective available potential energy (CAPE) and a level of neutral buoyancy (LNB) in the upper troposphere (for an undilute lifted parcel) is a necessary ingredient for the initiation of moist deep convection. However, it is insufficient even when convective inhibition (CIN) is negligible (e.g., Derbyshire et al. 2004; Khairoutdinov and Randall 2006; Houston and Niyogi 2007; Nelson et al. 2021). Thus, it is common to have widespread CAPE and little CIN but without any deep convection in a region. Over tropical oceans deep convective initiation typically involves growth of a cumulus congestus mode first (e.g., Johnson et al. 1999; Hohenegger and Stevens 2013a), whereas in the midlatitudes deep convection has been observed to often grow directly from a shallow mode (Zhang and Klein 2010). The progressive deepening of cumulus clouds is commonly referred to as the “shallow-to-deep” convective transition. This occurs as the convective thermals comprising cumulus clouds ascend to increasingly greater heights (e.g., Waite and Khouider 2010; Kirshbaum 2011).

Besides the obvious requirements of CAPE with a sufficiently high LNB and parcels being able to overcome any CIN, several mechanisms controlling deep convective initiation have been proposed. Numerous studies have focused on the role of free-tropospheric environmental relative humidity  $\phi_E$  (e.g., Brown and Zhang 1997; Sherwood and Wahrlich 1999; Sherwood 1999; Derbyshire et al. 2004; Takemi et al.

2004; Takayabu et al. 2010; Zhang and Klein 2010; Nelson et al. 2021; Tian et al. 2021). For example, a transition from the shallow to deep convective phase of the MJO occurs concurrently with an increase in  $\phi_E$  (e.g., Bladé and Hartmann 1993; Brown and Zhang 1997; Benedict and Randall 2007; Zermeño-Díaz et al. 2015; Chen and Zhang 2019). Sensitivity to  $\phi_E$  has also been observed for deep convective initiation in subtropical South America (Nelson et al. 2021) and over the Amazon (Tian et al. 2021). Based on an analysis of observations in the central United States,  $\phi_E$  was found to be a critical factor in explaining the growth of shallow cumulus into deep convection (Zhang and Klein 2010). This strong connection of deep convective initiation to  $\phi_E$  is primarily due to mixing processes (at least, for convection rooted in the boundary layer), since the “virtual” effect of moisture on air density and hence buoyancy is usually very small.

The prominent role of  $\phi_E$  in controlling deep convective initiation has led to the idea of moisture preconditioning being important (e.g., Johnson et al. 1999; Waite and Khouider 2010; Yano and Plant 2012). This is centered on the mechanism of earlier cumulus congestus clouds decaying and depositing moisture in the free troposphere, increasing  $\phi_E$  and providing a more favorable environment for subsequent convection to grow deep (Waite and Khouider 2010). However, the importance of this mechanism in the real atmosphere has been questioned by Hohenegger and Stevens (2013a) based on observational analysis. In the tropics, they found that the time scale for moistening by cumulus congestus ( $>1$  day) was too slow to explain the observed relatively rapid transition from congestus to deep convection (typically about 2 h over land

Corresponding author: H. Morrison, hmorrison@ucar.edu

DOI: 10.1175/JAS-D-21-0056.1

© 2022 American Meteorological Society. For information regarding reuse of this content and general copyright information, consult the AMS Copyright Policy ([www.ametsoc.org/PUBSReuseLicenses](http://www.ametsoc.org/PUBSReuseLicenses)).

and 4 h over ocean). Zhang and Klein (2010) also suggested that moisture preconditioning (from shallow cumulus) was likely not an important factor in midlatitudes, supported by additional analysis in Hohenegger and Stevens (2013b).

In cloud resolving model (CRM) simulation and large-eddy simulation (LES) of the shallow-to-deep convective transition over the Amazon, Grabowski et al. (2006) showed a relationship between a deepening planetary boundary layer forced by horizontally uniform surface fluxes, the width of clouds at their base, and the height they attained. Other studies have related deep convective initiation specifically to mesoscale dynamical features. In the LES study of Khairoutdinov and Randall (2006), also with horizontally homogeneous forcing, convection only grew deep after formation of precipitation leading to cold pools despite significant CAPE and almost no CIN. This behavior was attributed to cold pool circulations that were able to generate large enough thermals whose cores were protected from entrainment and dilution, in contrast to the smaller clouds prior to precipitation that were quickly wiped out by mixing and remained shallow. Several LES studies have similarly documented how cold pools modify convective properties and enhance vertical cloud growth by decreasing fractional entrainment rates and dilution (e.g., Kuang and Bretherton 2006; Schlemmer and Hohenegger 2014; Kurowski et al. 2018). Kuang and Bretherton (2006) noted that “the organized circulations of cold pools seem to create clouds with larger-sized bases and may correspondingly contribute to smaller lateral entrainment rates.”

Other papers have described how “external” forced ascent from large-scale convergence or mesoscale circulations, as opposed to features such as cold pools that are directly driven by convection itself, can initiate deep convection (e.g., Krueger 1988; Parsons et al. 1991; Xu et al. 1992; Bluestein and Parker 1993; Mapes and Houze 1995; Ziegler et al. 1997; Pielke 2001; Trier et al. 2004; Yuter et al. 2005; Masunaga and Kummerow 2006; Garcia-Carreras et al. 2011; Rieck et al. 2014; Rousseau-Rizzi et al. 2017). Besides mountainous terrain, other surface heterogeneities (e.g., in moisture) can promote horizontal gradients in virtual potential temperature and drive solenoidal circulations that initiate deep convection (e.g., Trier et al. 2004). Rousseau-Rizzi et al. (2017) analyzed deep convective initiation along a mesoscale convergence line in LESs forced by surface heat fluxes and also found that the height attained by cloud thermals was strongly correlated with the horizontal area of the nascent thermals. Broader circulations may contain more intense and concentrated (length scale of 1–10 km) PBL circulations that directly drive deep convective initiation, as has been simulated (Ziegler et al. 1997; Trier et al. 2004) and observed (Parsons et al. 1991; Atkins et al. 1998) in the central United States. Land–sea breezes in the tropics and midlatitudes provide a diurnally recurring forcing mechanism for deep convection (a well-known example is the near-daily “Hector” thunderstorm that occurs over the Tiwi Islands north of mainland Australia during the wet season).

Given the complexity of moist convection and its interactions with the environment, a single dominant mechanism controlling deep convective initiation is unlikely. Although previous studies have linked deep convective initiation to  $\phi_E$  or reduced lateral entrainment associated with wider updrafts

(e.g., Grabowski et al. 2006; Khairoutdinov and Randall 2006; Kuang and Bretherton 2006; Schlemmer and Hohenegger 2014; Rieck et al. 2014; Rousseau-Rizzi et al. 2017; Tian et al. 2021), details of the connections between updraft growth and structure, entrainment, and dilution remain unclear in this context. Improved understanding of these connections is a basic goal of the current study.

There have been recent advances in understanding with regard to moist convective dynamics more generally, largely driven by increased computing power and widespread use of LES models. A theme that has emerged from these studies is that cumulus clouds are often composed of discrete thermals<sup>1</sup> that rise in succession (e.g., Raymond and Blyth 1989; Blyth and Latham 1993; Damiani et al. 2006; Heus et al. 2009; Kirshbaum 2011; Moser and Lasher-Trapp 2017; Peters et al. 2020), termed “thermal chains” in Morrison et al. (2020). On a basic level, this explains the bubbling nature of cumulus clouds readily apparent, for example, from time lapse video. Modeling has suggested that, all else equal, relatively narrow convective clouds in a dry environment are more thermal-like while wider clouds in a moist environment are more plume-like (Morrison et al. 2020; Peters et al. 2020). Individual thermals comprising cumulus clouds are associated with localized pulses of enhanced entrainment associated with their toroidal circulations (Moser and Lasher-Trapp 2017; Morrison et al. 2020; Peters et al. 2020). Thus, some cloud regions can remain fairly undilute while the cloud as a whole undergoes considerable mixing and dilution. This is especially relevant to the problem of deep convective initiation because one might anticipate that the final height attained by a moist updraft is dictated by those cloud parcels that are relatively less dilute compared to other parts of the cloud. Here we cast the problem of deep convective initiation in this light to understand the driving mechanisms of cloud growth. Specifically, we address the following questions: 1) How do changes in  $\phi_E$  and updraft radius (in our simulations, controlled by the horizontal scale of surface flux forcing) influence whether or not convection goes deep? 2) How is this behavior modulated by changes in entrainment and dilution of buoyancy? 3) Can this behavior be reasonably described by a simple theoretical model of updraft buoyancy?

In this paper, we use a combination of theory and LES to address these questions. In section 2, we apply a theoretical analysis of moist updraft dynamics to develop a “scale selection” hypothesis proposing that shallow clouds grow deep only when the horizontal scale of subcloud ascent exceeds a  $\phi_E$ -dependent threshold length scale. In section 3 we describe the setup and experimental design of the LESs. Section 4 discusses the main results including evaluation of the scale selection hypothesis and comparison of the theoretical and LES results. A brief summary and conclusions are given in section 5.

<sup>1</sup> By “discrete thermals,” we mean flow features that are positively buoyant relative to their surroundings and have distinctive toroidal circulations. These features have a length scale similar to the cloud width as a whole, as opposed to the ubiquitous smaller-scale turbulent eddies associated with cumulus clouds.

## 2. Theoretical description

A theoretical model describing the thermodynamic and dynamic behavior of moist convective updrafts was developed by Morrison (2017, hereafter M17) and extended in Morrison et al. (2020, hereafter M20). We utilize this simple model to develop a theoretical description of cumulus clouds focusing on the height obtained by ascending buoyant updrafts. A detailed derivation of the model is presented in M20 and only briefly described here. We focus on expressions for the evolution of a passive tracer  $C$  and buoyancy  $B$  in the updraft core in an axisymmetric  $(r, z)$  coordinate system. Note that we do not assume any particular updraft structure (e.g., steady-state plumes); this issue is elaborated upon below. The model applies a first-order eddy diffusion scheme to represent lateral mixing of  $C$  as described in M17 and M20 (similar to Kuo 1962; Asai and Kasahara 1967; De Rooy and Siebesma 2010) to give

$$\frac{dC}{dz} = -\frac{2k^2L}{P_r R^2}(C - C_E) = -\varepsilon(C - C_E), \quad (1)$$

where we define a bulk fractional entrainment rate (units of inverse length) as

$$\varepsilon \equiv \frac{2k^2L}{P_r R^2}. \quad (2)$$

Here  $k$  is a scaling constant,  $P_r$  is the Prandtl number,  $L$  is a turbulent mixing length,  $R$  is the updraft radius,  $z$  is height, and  $C_E$  is the value of  $C$  in the environment. Equation (1) represents the Lagrangian evolution of  $C$  in the updraft core ( $r = 0$ ) as a function of height for a parcel just below cloud top, which is valid since the cloud's top is assumed to rise at the rate of the local vertical velocity  $w$  (i.e., the  $w$  at cloud top). This expression is derived by approximating the horizontal turbulent flux divergence of  $C$  as  $(2K_C/L)(\partial C/\partial r)$  where  $K_C = (k^2 L^2/P_r)|\partial w/\partial r|$  is a turbulent diffusion coefficient (see M20 for details). Horizontal derivatives of  $w$  and  $C$  are approximated using a simple linear horizontal difference operator giving  $\partial w/\partial r \approx -w/R$  and  $-\partial C/\partial r \approx (C - C_E)/R$ , where  $w = 0$  and  $C = C_E$  at the updraft lateral edge ( $r = R$ ). In the divergent flow near the updraft top, we assume that any organized detrainment (dynamic detrainment) does not affect core properties. We also neglect vertical mixing, which is expected to be important right at cloud top but less important just below cloud top given weaker vertical gradients there (see discussion M20). Note that M17 and M20 also developed expressions for updraft core  $C$  and  $B$  in the convergent flow lower in the cloud accounting for dynamic entrainment where  $\partial w/\partial z > 0$ . However, because we are specifically concerned about core properties in the divergent flow near cloud top, these expressions are not used here.

Note that here  $\varepsilon$  is an *implied* fractional entrainment rate; in other words, it is the bulk fractional entrainment rate needed to produce dilution of  $C$  consistent with (1). This differs from the fractional entrainment rate obtained from “direct” methods applied to LES (Romps 2010; Dawe and Austin 2011) that calculate  $\varepsilon$  as the mass flux across a cloudy updraft edge divided by the upward mass flux. These direct methods do not make

any assumptions about the properties of entrained air, unlike bulk methods [as implied by the factor of  $(C - C_E)$  in (1)], and thus can differ from bulk estimates by up to about a factor of 2 (Romps 2010). However, because we are concerned with core dilution rather than the mass flux across the updraft boundary per se (particularly the dilution of buoyancy since it is critical for determining the termination height of ascending updrafts), in this study we focus on the bulk  $\varepsilon$ .

Using  $C = C_{\text{LFC}}$  as the lower boundary condition and  $C_E = 0$  consistent with initialization of the passive tracer in the LES described later, and assuming  $L$  and  $R$  are constant along the rising cloud element, (1) can be easily integrated to give an analytic expression for  $C$  as a function of the rising cloud-top height:

$$C = C_{\text{LFC}}e^{-\varepsilon z}. \quad (3)$$

There is no general theory for  $L$  applicable to moist atmospheric convection.<sup>2</sup> For simple turbulent flows (dry, Boussinesq, homogeneous environment),  $L$  is expected to scale with the length of the flow feature, such as radius of a thermal, for dimensional consistency. Assuming that  $L$  is proportional to  $R$  (e.g., Asai and Kasahara 1967) in (2) and (3) gives the classical  $R^{-1}$  scaling of  $\varepsilon$  from dimensional analysis and laboratory studies of *dry* plumes and thermals (Morton et al. 1956; Turner 1957). However, it is unclear if such scaling of  $L$  is appropriate for *moist* atmospheric convection, which has additional length scales associated with stratification, moisture, and PBL depth, among others. We use values of  $L$  in (2) and (3) that give the best fit for  $C$  compared to the LES results (see section 4c). We obtained best-fit values assuming either constant  $L$  or  $L \propto R$ ; a constant  $L = 120$  m gives somewhat closer values than the best-fit  $L \propto R$  as detailed in section 4c (note there is little sensitivity of the best fit value of  $L$  to doubling the LES model grid length, see section 3). This is consistent with recent studies showing that bulk dilution of LES deep moist updrafts using is better described using a constant  $L$  in (2) and (3), giving  $\varepsilon \propto R^{-2}$  (Peters et al. 2019; Mulholland et al. 2021). Thus, we use  $L = 120$  m in our simple model in this study, except as noted.

A similar approach is used to derive an expression for core buoyancy near the cloud top. This is more complicated because buoyancy is not a passive tracer and is influenced by many processes that impact local density. For simplicity we only include the effects of changes in temperature on buoyancy; the effects of condensate loading, water vapor perturbations, and pressure perturbations are neglected.

M17 derived an expression for condensation rate as a function of local  $w$  [Eqs. (12)–(23) therein]. The lateral turbulent mixing of temperature  $T$  and water vapor mixing ratio  $q_v$  was treated similarly to the mixing of  $C$  [Eq. (15) in M17]. From the condensation rate, expressions were obtained for the local latent heating and the buoyancy tendency  $dB/dt$  near

<sup>2</sup> Note that  $L$  in this context is for mixing associated with all scales of turbulence. This is different from the mixing length for subgrid-scale turbulence in the LES model, which is discussed in section 3.

the cloud top as it ascends in M20. A substitution was then made by applying the chain rule  $[dB/dt = (dB/dz)(dz/dt) = (dB/dz)w]$  and dividing the resulting equation by  $w$  to give (see M20 for details):

$$\frac{dB}{dz} = \underbrace{gQ}_{\text{term 1}} - \underbrace{\varepsilon B}_{\text{term 2}} - \underbrace{\frac{gL_v q_{sE}(1 - \phi_E)\varepsilon}{c_p T_E \Gamma}}_{\text{term 3}}, \quad (4)$$

where  $g$  is gravitational acceleration,  $\Gamma = 1 + (L_v/c_p)(dq_s/dT) \approx 1 + L_v^2 q_{sE}/(c_p R_v T_E^2)$ ,  $L_v$  is the latent heat of vaporization,  $q_{sE}$  is the saturation mixing ratio of the environment,  $T_E$  is the temperature of the environment,  $c_p$  is the specific heat of air at constant pressure,  $R_v$  is the gas constant for water vapor, and  $Q$  is the difference between the moist adiabatic and environmental lapse rates divided by  $T_E$  (equal to the change in  $B$  with height for a moist pseudoadiabatically lifted parcel divided by  $g$ , where only temperature is considered for buoyancy). On the right-hand side of (4) “term 1,” “term 2,” and “term 3” are, respectively, 1) change in buoyancy from pseudoadiabatic moist ascent, 2) change in buoyancy from lateral mixing of dry static energy between updraft and dry environment air, and 3) decrease in buoyancy from water phase changes with lateral mixing of updraft and dry environment air. Note that (4) is identical to (18) in M17 [it appears different only because here we use  $\varepsilon$  as a shorthand for writing out  $2k^2 L/(P_r R^2)$ ].

A noteworthy feature of the expressions for both  $C$  and  $B$  above is that they do not explicitly depend on  $w$ . This occurs because faster ascent and less time for dilution with stronger  $w$  is countered by greater shear production of turbulence and stronger mixing. With our formulation of the mixing term above, the two exactly balance and  $w$  divides out of the equations. Thus,  $\varepsilon$  does not depend on  $w$ , which is counter to some studies that have suggested that  $\varepsilon$  should scale with  $w^{-1}$  (e.g., Neggers et al. 2002; Anber et al. 2019). Nonetheless, if one integrates the  $B$  Eq. (4) above to estimate  $w^2$ , there is a strong negative correlation between  $w$  and  $\varepsilon$  because of greater dilution as  $\varepsilon$  increases (see section 4 of M20). Thus, we argue that an inverse relationship between  $w$  and  $\varepsilon$  may at least in part reflect the direct impact of  $\varepsilon$  on dilution and hence  $w$ , rather than the impact of  $w$  on  $\varepsilon$ . Because there is no direct dependence of our expressions for  $C$  and  $B$  above on  $w$ , the well-known scaling of adverse perturbation pressure forcing with buoyant updraft aspect ratio (e.g., Morrison 2016; Peters 2016; Jeevanjee 2017) has no impact on the scaling of  $B$  and  $C$  with  $R$  here.

Squires and Turner (1962) also developed a simplified one-dimensional model calculating profiles of vertical mass flux, buoyancy, condensate,  $w$ , and  $R$ . They used this model to examine sensitivity of cloud-top height to various parameters including cloud base mass flux and  $\phi_E$ . Their model assumed an updraft structure of steady state, horizontally homogeneous plumes. From this basic assumption, they independently evolved vertical mass flux and plume  $w$  which allowed for diagnosing a height-varying  $R$ . In contrast, we do *not* assume steady state plumes given numerous observational (e.g., Raymond and Blyth 1989; Blyth and Latham 1993; Damiani et al. 2006; Yeung et al. 2021) and LES (e.g., Heus

et al. 2009; Kirshbaum 2011; Moser and Lasher-Trapp 2017; Peters et al. 2020) studies that have highlighted the thermal-like structure of moist convection, as noted in the introduction. The only assumption we make regarding updraft structure is that the  $R$  of rising cloud elements is constant in a Lagrangian sense. This follows from the seminal study of Arakawa and Schubert (1974, p. 683), who noted “The assumption that  $R$  is constant with height, in the Lagrangian sense, leads to better agreement with observations than the alternative assumptions of horizontally expanding thermals or starting plumes . . . . In our model, also, we assume that  $R$  is constant with height in the Lagrangian sense.” More recent work tracking cloud thermals in LES has verified nearly constant  $R$  of tracked thermals as they rise (Hernandez-Deckers and Sherwood 2016, 2018), further supporting this assumption.

M17 obtained a fully analytic approximate solution to (4) as a function of  $z$  by assuming a linear profile of  $B$  above the LFC, where  $B$  is assumed to be zero. Here solutions for  $B$  are also obtained by numerically integrating (4), and we compare these solutions to the analytic approximation from M17. The thermodynamic sounding for the calculations is the analytic profile from Weisman and Klemp (1982, hereafter WK82) with a surface vapor mixing ratio of  $14 \text{ g kg}^{-1}$ , modified as described in section 3. In the calculations we use  $k^2 = 0.178$  and  $P_r = 1/3$  following M17 and M20, and  $L = 120 \text{ m}$  as described above. The pseudoadiabatic buoyancy for the calculations is based on ascent of the parcel with maximum CAPE. To integrate (4) numerically we use a simple forward Euler approach with a vertical spacing of  $100 \text{ m}$  with a lower boundary condition of  $B = 0$  at the LFC. Despite its simplicity this method provides sufficient accuracy. Degrading the vertical grid spacing to  $200 \text{ m}$  and recalculating the  $B$  profiles described below results in a maximum error of 7% relative to the  $100 \text{ m}$  calculation (for points with  $B \geq 0.01 \text{ m s}^{-2}$ ), with the vast majority of points having error  $< 1\%$ .

Results are shown in Fig. 1 for dry ( $\phi_E = 0.425$ , Figs. 1a–c) and humid ( $\phi_E = 0.85$ , Figs. 1d–f) environments for three different values of  $R$  (0.55, 1, and 1.5 km). The analytic approximation for  $B$  from M17 and numerical solution from integrating (4) give similar profile shapes and responses to changes in  $R$  and  $\phi_E$  (cf. the blue and red lines in Fig. 1). The analytic approximation gives larger  $B$  than the numerical calculations, mainly above the buoyancy peak, leading to overestimation by up to  $\sim 3 \text{ km}$  of the height where buoyancy returns to zero – the updraft’s equilibrium height  $z_B$ . Despite this, the difference in vertically integrated buoyancy is relatively small ( $< 15\%$  of CAPE). We will use the numerical approach for solving (4) hereafter.

For the ranges of  $\phi_E$  and  $R$  considered, there is substantial dilution of  $B$  relative to the pseudoadiabatic value (cf. the red lines and black dotted lines in Fig. 1). The dilution of  $B$  increases as  $R$  or  $\phi_E$  decrease. The influence of  $R$  is through its impact on  $\varepsilon$  and hence entrained mass, whereas  $\phi_E$  affects the reduction in buoyancy per unit entrained mass through its impact on water phase changes. The height of maximum  $B$  is influenced by mixing and dilution and increases with  $R$  and  $\phi_E$ . For instance, this height is  $\sim 2.5 \text{ km}$  for  $R = 0.7 \text{ km}$  and

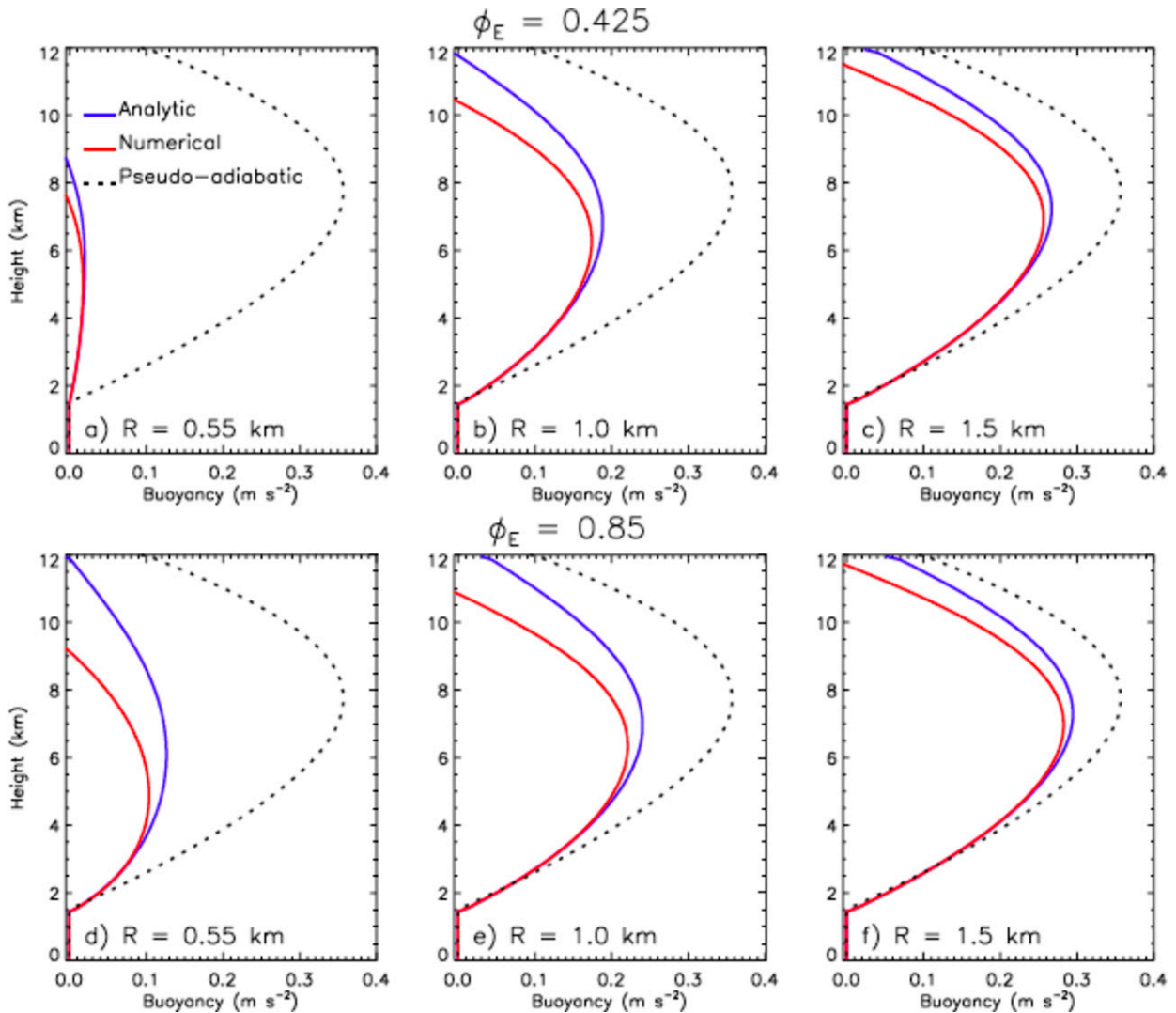


FIG. 1. Vertical profiles of updraft-core buoyancy from the analytic approximation (blue lines), numerical integration of the theoretical expression (4) (red lines), and undilute ascent (dotted black lines). Results are for  $\phi_E$  of (a)–(c) 0.425 and (d)–(f) 0.85. Updraft radii  $R$  is varied from 0.5 km in (a) and (d), to 1.0 km in (b) and (e), and to 1.5 km in (c) and (f).

$\phi_E = 0.425$ , compared to a height of maximum pseudoadiabatic  $B$  of 7.5 km.

Because this study is concerned with deep convective initiation, we plot  $z_B$  as a function of  $R$  and  $\phi_E$  (Fig. 2a). We focus on  $z_B$  as a simple measure of cloud updraft height since it is readily calculated by integrating (4) and avoids complications with updrafts overshooting their equilibrium level. The effects of increased  $B$  dilution, leading to reduced  $z_B$  with decreasing  $R$  and/or  $\phi_E$ , are clearly seen in the figure. The WK82 thermodynamic sounding used in the calculations has fairly steep mid-tropospheric lapse rates and thus large pseudoadiabatic buoyancy. Modifying the lapse rate to uniformly reduce the pseudoadiabatic buoyancy by a factor of 4 while maintaining the same LNB (thus, reducing CAPE by a factor of 4) leads to greater sensitivity of  $z_B$  to  $\phi_E$  (Fig. 2b). This occurs because the generation of buoyancy by ascent is unable to overcome

the deleterious effects of mixing with dry air as the pseudoadiabatic buoyancy is decreased. This result is consistent with the modeling study of Houston and Niyogi (2007). Our results also suggest that a more humid environment is needed for deep convective initiation when lapse rates are relatively weak and hence pseudoadiabatic buoyancy is small.

A sharp transition from shallow ( $z_B < 3$  km) to deep convection ( $z_B > 8$  km) occurs with an increase in  $R$  of less than a few hundred meters for both the standard WK82 and reduced CAPE soundings (Fig. 2). An increase in  $z_B$  with cloud base  $R$  was also found by Squires and Turner (1962), but with a much smaller effect of changes in  $R$ . This difference likely reflects the use of different modeling frameworks, particularly the assumption of a steady state plume in Squires and Turner (1962). The sharp transition with  $R$  here is consistent with the LESs of Rousseau-Rizzi et al. (2017), who

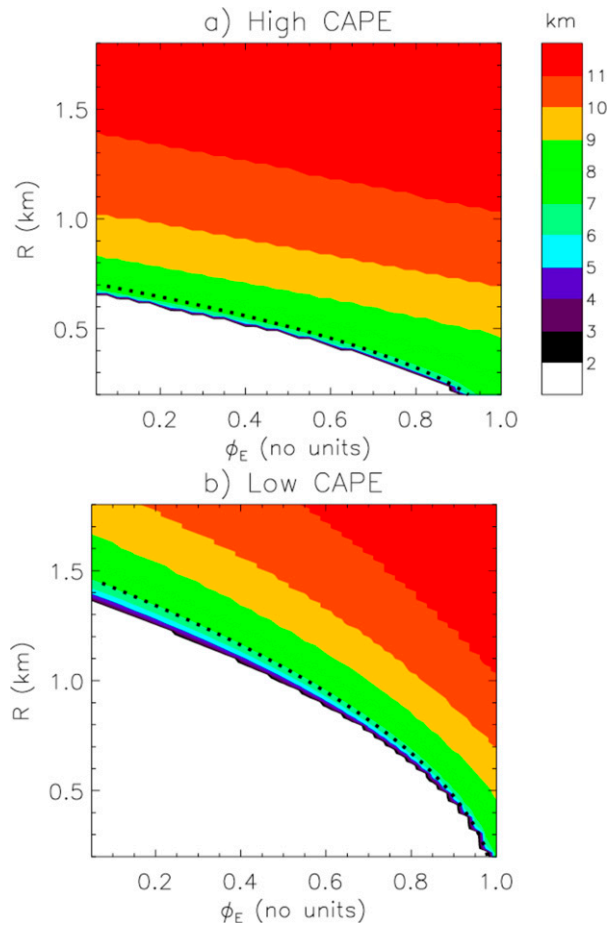


FIG. 2. Updraft equilibrium buoyancy height  $z_B$  as a function of environmental relative humidity  $\phi_E$  ( $x$  axis) and updraft radius  $R$  ( $y$  axis) from numerically integrating the theoretical expression for  $dB/dz$  given by (4). Results are for the WK82 thermodynamic sounding (a) with high CAPE ( $\sim 2600 \text{ J kg}^{-1}$ ) and (b) with a reduced lapse rate corresponding to lower CAPE ( $\sim 650 \text{ J kg}^{-1}$ ), but the same LFC and LNB. Dotted black lines show constant values of the ratio  $R^2/(1 - \phi_E)$  indicating the threshold for deep convective initiation, with this ratio equal to 0.52 in (a) and 2.25 in (b).

showed an average increase of 4–5 km in the height attained by cloud thermals with an increase in thermal horizontal area  $A$  at the LFC from about 0.1 to 0.35  $\text{km}^2$  (e.g., see Fig. 10 therein); this corresponds to an increase in  $R$  of  $\sim 150 \text{ m}$  assuming  $R = \sqrt{A/\pi}$ . Here this behavior is explained by analyzing the three terms on the right-hand side of the  $dB/dz$  equation. Term 3—the change in buoyancy from mixing of cloud and environmental air and associated water phase changes—is always negative (buoyancy sink). Between the sounding’s LFC and level of maximum pseudoadiabatic  $B$  (here, at 7.5 km), term 1—the change in buoyancy from pseudoadiabatic ascent—is always positive, i.e., a buoyancy source. Term 2—lateral mixing of dry static energy—is negative between the LFC and  $z_B$  where  $B > 0$ .

Figure 3 shows each of the three terms in the  $dB/dz$  equation as  $R$  is varied as well as these terms integrated over height. These

calculations use  $\phi_E = 0.425$ . We show results using both the standard WK82 sounding (Figs. 3a,b) and the one with CAPE reduced by a factor of 4 (Figs. 3c,d). At the transition where  $z_B$  increases sharply, term 2 (proportional to  $B$ ) is small compared to terms 1 and 3. Thus, the buoyancy profile below  $\sim 6\text{--}7 \text{ km}$  is determined mostly by a balance between production via term 1 and loss via term 3. Magnitudes of terms 1 and 3 decrease with height similarly between the LFC and  $\sim 6\text{--}7 \text{ km}$  so that the buoyancy is nearly constant with height for values of  $R$  where the transition occurs (i.e., the sum of the terms equal to  $dB/dz$  is close to zero). This means that increasing dry air entrainment from a small decrease in  $R$  can push the buoyancy from being small but positive over a deep layer from the LFC to  $\sim 6 \text{ km}$  to being small but negative over this layer, leading to a sharp decrease in  $z_B$ . Compensation of terms 1 and 3 is a general feature and occurs because both terms depend similarly on the moist adiabatic lapse rate. Given this compensation, the ratio of terms 1 and 3 is approximately constant with height from the LFC to  $\sim 6 \text{ km}$ . The transition to deep convection occurs when the absolute value of this ratio  $> 1$ , that is, when magnitude of term 1 is larger than that of term 3. Writing out these terms following (4) and (2), this implies that deep convective initiation occurs approximately when  $R^2/(1 - \phi_E)$  is greater than a threshold value that depends on the environmental lapse rate above the LFC. In other words, the height attained by an updraft depends on the ratio of horizontal updraft area ( $\propto R^2$ ) to saturation deficit of the environment ( $1 - \phi_E$ ); for a given lapse rate, as the saturation deficit decreases there is a corresponding decrease in the minimum updraft area required for the updraft to grow deep. Indeed, the transition to deep convection (sharp increase in  $z_B$ ) calculated from integrating the full buoyancy equation closely follows this simple scaling threshold (see Fig. 2).

As noted above, the sharp transition to deep convection with increasing  $R$  occurs because the magnitudes of terms 1 and 3 in the  $dB/dz$  equation decrease with height at a similar rate. Thus, soundings that have a much faster decrease of  $B_{AD}$  (i.e., term 1) with height—those with so-called bottom-heavy CAPE profiles—may have a smoother increase of  $z_B$  with  $R$ . Also note that the  $R^2$  dependence for the scaling describing the shallow to deep transition comes from the assumption that  $L$  is a constant in (2). Assuming instead that  $L \propto R$  changes the scaling (i.e., the dotted black lines in Fig. 2) from parabolic to linear in  $R$  (not shown). However, this does not change the overall picture, particularly the sharpness of the transition from shallow to deep. The idea of a minimum horizontal cloud base area being required for deep convection was previously suggested by Grabowski et al. (2006), Rochetin et al. (2014), and Rousseau-Rizzi et al. (2017) based on CRM and LES results. Our analysis formalizes this concept and describes how the threshold scale depends on saturation deficit and cloud layer lapse rate.

Although the theoretical expressions above are in terms of updraft radius  $R$ , we frame the problem in terms of the horizontal scale of subcloud ascent,  $R_{\text{sub}}$ . As we show in section 4,  $R_{\text{sub}}$  is directly driven by the imposed horizontal scale of surface flux forcing in our LESs, and in turn it strongly influences the cloud width while being mostly independent of how the

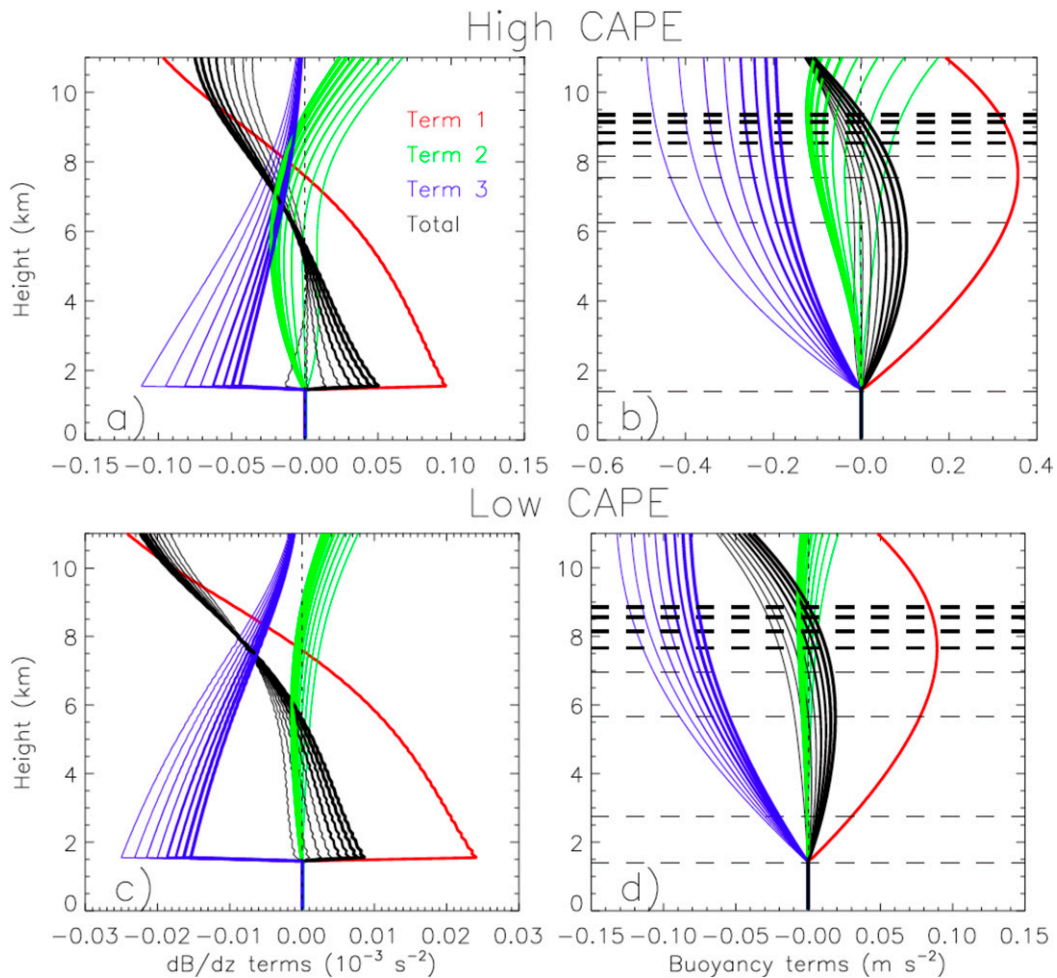


FIG. 3. Vertical profiles of (a),(c) terms in the  $dB/dz$  equation given by (4); (b) (d) these terms integrated over height. Terms 1 (red), 2 (green), and 3 (blue) are, respectively, buoyancy change from pseudoadiabatic moist ascent, buoyancy change from lateral mixing of dry static energy between environment and updraft air, and buoyancy sink from water phase changes associated with lateral mixing of cloudy and dry environmental air. (a),(b) Results for the standard WK82 sounding with high CAPE; (c),(d) results for the modified WK82 sounding with reduced lapse rate and CAPE decreased by a factor of 4. Solid black lines indicate the sum of the three terms (total) equal to  $dB/dz$  in (a) and  $B$  in (b). Thin dotted vertical lines show the zero line. Lines of different thicknesses show results for different updraft radii  $R$  every 40 m between 480 m (thinnest lines) and 760 m (thickest lines). Term 1 is independent of  $R$  and thus shown only by a single line. Horizontal black dashed lines in (b) and (d) show the height of equilibrium buoyancy  $z_B$  for the different  $R$  values. The value of  $\phi_E$  is 0.425 and all other parameters are specified as described in section 2.

cloud evolves. From this connection and our theoretical results, we propose a “scale selection” hypothesis for the initiation of deep moist convection: *In environments potentially supporting deep convection, the transition to deep convection occurs when coherent vertical motion up to the LFC exceeds a certain horizontal scale, and this threshold scale increases as the  $\phi_E$  decreases.* Specifically, the ratio of  $R_{\text{sub}}^2$  to saturation deficit  $(1 - \phi_E)$  must exceed a certain threshold value that depends on cloud-layer environmental lapse rate. A transition to deep convection is, of course, also conditional on the thermodynamic profile having CAPE with a sufficiently high LNB and parcels being able to overcome any CIN. Also note that Fig. 2 represents the equilibrium height of buoyant updrafts; at

any specific time cloud top may be below this height but actively ascending.

### 3. Description of numerical model and experimental setup

The LESs in this study use the Cloud Model version 1 (CM1). CM1 is a nonhydrostatic, compressible model well suited for simulating idealized atmospheric flow (Bryan and Fritsch 2002). Microphysical processes follow from Morrison et al. (2009), but for simplicity precipitation generation and ice processes are turned off so that only cloud condensation and evaporation following “saturation adjustment” are included. For simplicity and

consistency with the theoretical model, condensate and water vapor virtual effects are neglected in the buoyancy. The 1.5-order TKE-based scheme from [Deardorff \(1980\)](#) is used for subgrid-scale mixing. We use the standard configuration of this scheme in CM1, which calculates the subgrid-scale mixing length from the square root of the ratio of TKE to moist Brunt Vaisala frequency [see Eq. (10) in [Deardorff 1980](#)] in statically stable conditions. This effectively reduces the subgrid scale mixing under stable stratification. Under neutral or statically unstable conditions the mixing length is set to the model grid length, which is also the maximum allowed value for statically stable conditions. Radiation is neglected.

The domain size is  $18 \times 18 \times 18 \text{ km}^3$ , except as noted. In all LESs the upper and lower boundary conditions are free slip and rigid. Lateral boundary conditions are periodic. A Rayleigh damping layer is applied above 15 km. Grid cells are isotropic with a grid spacing of 50 m in each direction. The time step is 0.75 s.

Initial thermodynamic conditions are from the analytic temperature and water vapor mixing ratio profiles of [WK82](#), with a surface vapor mixing ratio of  $14 \text{ g kg}^{-1}$ . Initial winds are set to zero. To facilitate spin up of boundary layer turbulence, random perturbations ( $\pm 0.1 \text{ K}$ ) uncorrelated across grids are applied to the initial potential temperature field. We have modified the original [WK82](#) sounding by adjusting  $\phi_E$  above 2 km, about 0.5 km above the LFC. This adjustment is done by modifying the water vapor mixing ratio while keeping the temperature fixed. Relative humidity is not modified below 2 km to retain the same LFC. Since water vapor is neglected in the model's buoyancy calculation here, these changes have no impact on CAPE. Moreover, the modified  $\phi_E$  above 2 km is well above the PBL top (by several hundred meters) throughout the simulations, and thus does not directly affect what is entrained into the PBL. Initial  $\phi_E$  above 2 km is set to a constant in each run, with values of 0.3, 0.6, or 0.9. To analyze cloud dilution we initialize all LESs with a passive tracer having a value of  $1 \text{ kg kg}^{-1}$  below 1.5 km and zero elsewhere.

The general model setup follows the cumulus congestus case from the 10th International Cloud Modeling Workshop ([Shima and Grabowski 2021](#)), applied previously in [Grabowski \(2020\)](#) and [Chandrakar et al. \(2021\)](#). Boundary layer turbulence is spun up by applying horizontally uniform surface thermal ( $U_s$ ) and water vapor fluxes ( $U_l$ ) for the first hour. In all LESs  $U_s = 0.03 \text{ K m s}^{-1}$  and  $U_l = 1.2 \times 10^{-5} \text{ kg kg}^{-1} \text{ m s}^{-1}$  (equivalent to sensible and latent heat fluxes of approximately  $35 \text{ W m}^{-2}$  each). After one hour a Gaussian shaped horizontal distribution of surface fluxes with maximum values in the domain center is added to the uniform fluxes, which initiates moist convection. The surface thermal and vapor fluxes are given by

$$\begin{aligned} H_s &= U_s, & t < 3600 \text{ s} \\ H_l &= U_l, & t < 3600 \text{ s} \\ H_s &= U_s + M_s e^{-r^2/L_h^2}, & t \geq 3600 \text{ s} \\ H_l &= U_l + M_l e^{-r^2/L_h^2}, & t \geq 3600 \text{ s} \end{aligned} \quad (5)$$

where  $t$  is the simulation time,  $M_s = 0.3 \text{ K m s}^{-1}$  and  $M_l = 1.2 \times 10^{-4} \text{ kg kg}^{-1} \text{ m s}^{-1}$  are maximum surface thermal and vapor fluxes of the Gaussian distribution (equivalent to

TABLE 1. An overview of the main LESs discussed in this paper, where  $L_H$  and  $\phi_E$  indicate the length scale of surface flux forcing and initial environmental relative humidity above 2 km, respectively.

$L_H$ (m)	$\phi_E$	Integration time (h)
1000	0.3	3
1500	0.3	6
2500	0.3	3
3250	0.3	3
4000	0.3	3
1000	0.6	3
1500	0.6	3
2500	0.6	3
4000	0.6	3
1000	0.9	3
1500	0.9	3
2500	0.9	3
4000	0.9	3

sensible and latent heat fluxes of approximately  $350 \text{ W m}^{-2}$  each),  $r$  is the horizontal distance from the domain center, and  $L_H$  is a horizontal scale of the fluxes equal to  $\sqrt{2}$  times the standard deviation of the distribution. The surface flux forcing comes from the 10th International Cloud Modeling Workshop ([Shima and Grabowski 2021](#)) case following [Lasher-Trapp et al. \(2005\)](#). This forcing is strong and on the high end of total surface sensible plus latent heat flux observations (e.g., [Negggers et al. 2003a](#)), though comparable to that used in a previous shallow cumulus LES case study ([Negggers et al. 2003b](#)). In our tests  $L_H$  is set to 1000, 1500, 2500, or 4000 m. To better resolve sharp transitions in  $z_B$  as  $L_H$  is varied, additional runs with  $L_H = 3250 \text{ m}$  are included for the  $\phi_E = 0.3$  set.

A summary of the main simulations is given in [Table 1](#). To improve robustness, small three-member ensembles are run for each configuration to generate different realizations. Different members use different random number seeds for the small-amplitude initial potential temperature perturbations. All analysis is based on model data output every 5 min.

In addition to the main experiments listed in [Table 1](#), a handful of additional LESs were performed with the horizontal domain length doubled from 18 to 36 km. This increase in domain size does not qualitatively impact the main results, and does not affect our conclusions.

Finally, we examined sensitivity to grid resolution. A set of tests was run with the horizontal and vertical grid spacings increased from 50 to 100 m (decreasing the grid spacing below 50 m was not computationally feasible). We ran one realization each for the tests with varying  $L_H$  and  $\phi_E$ , and results are similar to the 50-m-grid-spacing simulations. In particular, the equilibrium cloud height  $z_B$  is within or very close to the ensemble spread of the 50-m simulations, and thus our main conclusions are insensitive to doubling the horizontal and vertical grid spacings. Also, the best fit  $L$  based on comparing  $C$  from our simple theoretical model with the LES increases only slightly from 120 to 138 m with a doubling of the model grid spacing from 50 to 100 m.

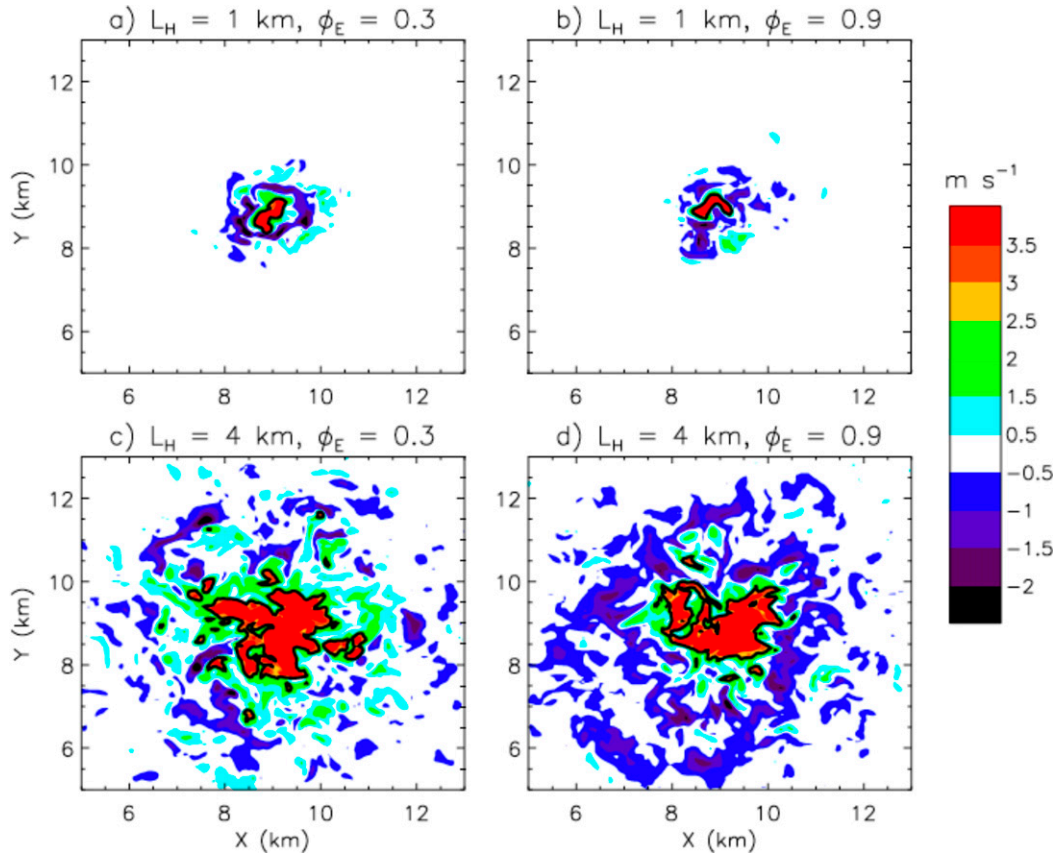


FIG. 4. Horizontal cross sections of subcloud vertical velocity (1-km height and 120 min) from four of the LESs. The horizontal length scale of the surface flux forcing  $L_H$  and environmental relative humidity  $\phi_E$  for each simulation is indicated above the plots. The solid black line shows the  $2 \text{ m s}^{-1}$  contour that defines the area of subcloud ascent as discussed in the text. Note that only part of the model horizontal domain is shown.

## 4. Results

### a. LES moist convection properties

The prescribed surface fluxes generate an organized region of ascent within the boundary layer after 60 min (Fig. 4), with maximum subcloud vertical velocities up to  $\sim 5\text{--}8 \text{ m s}^{-1}$ . The horizontal length scale of this ascent is determined by the horizontal length of the Gaussian-distributed surface flux forcing,  $L_H$ . Compensating descent with minimum velocities of about  $-2$  to  $-3 \text{ m s}^{-1}$  occurs along the periphery of the organized ascent. Because the surface fluxes are fixed in time after 1 h and there is no precipitation generation or cold pools, the characteristics of this subcloud circulation do not vary much over time once it is established. Moist convection begins in all runs between 90 and 100 min as the surface flux-driven circulation strengthens. This occurs as the cloud thermals rise from the LFC above the region of subcloud ascent. This behavior is illustrated by vertical cross sections of the vertical velocity, buoyancy, and cloud boundary at different times from a subset of the LESs (Figs. 5 and 6). We show only one realization per configuration but others produced similar results.

In LESs with the dry ( $\phi_E = 0.3$ ) environment and  $L_H = 1.5$ -km radius, new thermals rise from the LFC but rapidly

decay above  $\sim 3$  km before the next thermal emerges (Fig. 5, left column). This pulsing of thermal generation and decay is also evident in profiles of maximum  $w$  and  $B$  in the horizontal plane between 100 and 135 min (Fig. 7, blue lines). For example, at 105 min there is a brief pulse of  $w$  exceeding  $7 \text{ m s}^{-1}$  near 3.5-km height that decays by 110 min. The run with a larger radius ( $L_H = 2.5$  km) in the same environment also produces this pulsating behavior (Fig. 5, right column). The primary thermal circulations as well as the cloud itself are broader, and the thermals ascend much higher, than in the run with the smaller radius. However, these thermals still rapidly decay above 7 km and experience substantial negative buoyancy as seen in Fig. 5f.

The general character of the convection is quite different in the moist ( $\phi_E = 0.9$ ) environment. With a large radius ( $L_H = 4$  km), a starting-plume-like<sup>3</sup> feature ascends through the depth of the troposphere between 95 and 115 min, evident in profiles of horizontal maximum  $w$  and  $B$  (red lines in Fig. 8).

<sup>3</sup> A starting plume consists of a thermal-like structure at the head of an ascending plume, with the flow behind the head resembling a steady-state plume (Turner 1962).

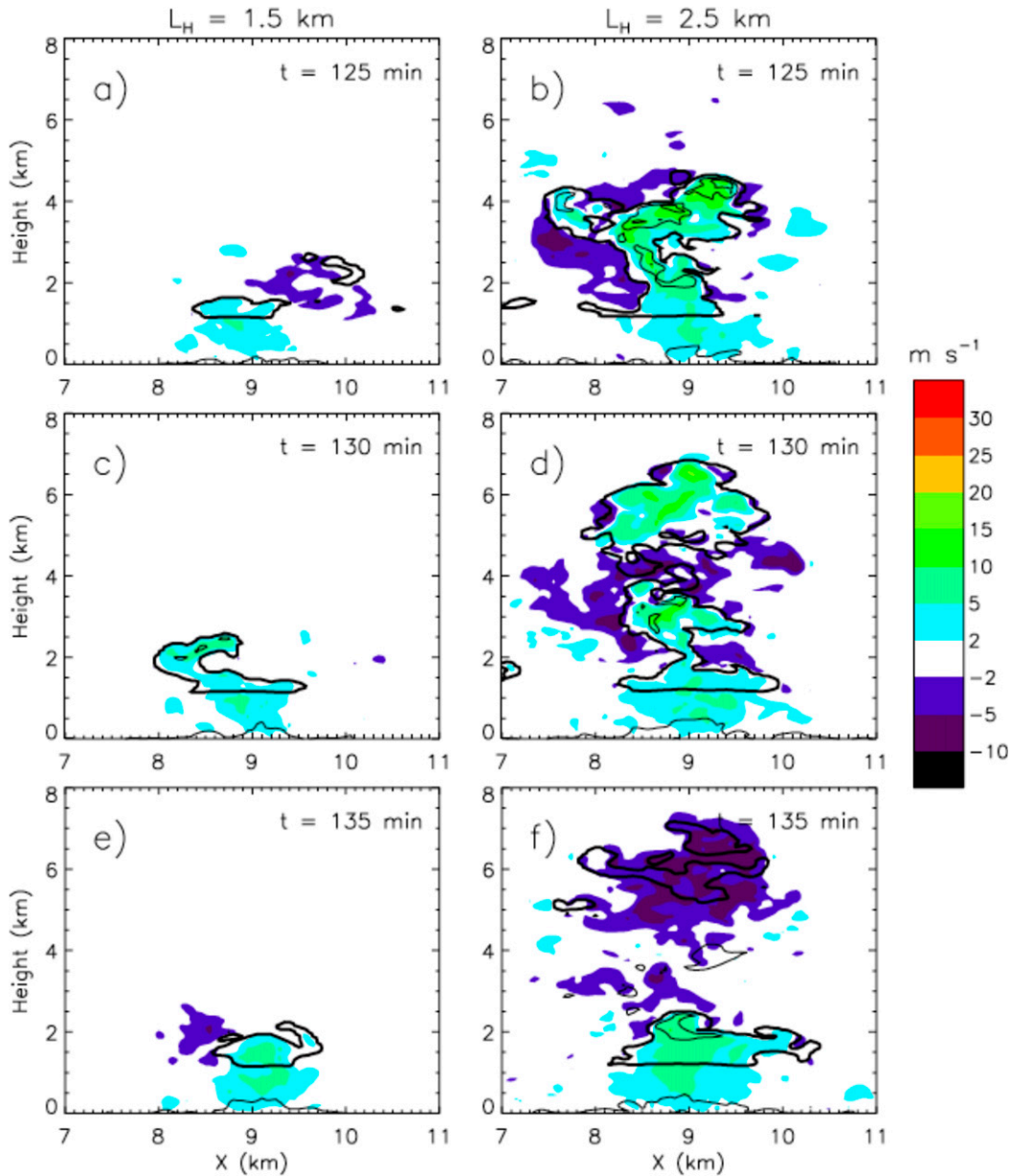


FIG. 5. Vertical cross sections of buoyancy (thin black contour lines, intervals of  $0.05 \text{ m s}^{-2}$  starting with  $0.05 \text{ m s}^{-2}$ ), vertical velocity (color contours as labeled), and cloud boundaries (thick black lines, defined by cloud water mixing ratio  $\geq 0.1 \text{ g kg}^{-1}$ ) for LESs with  $\phi_E = 0.3$  and (a),(c),(e)  $L_H = 1.5 \text{ km}$  or (b),(d),(f)  $L_H = 2.5 \text{ km}$  at the times indicated.

Thereafter the updraft structure is fairly steady and has generally increasing  $w$  from the LFC to 8–10 km, resembling a plume, in contrast to the LESs with lower  $\phi_E$  and smaller  $L_H$ . There are small localized peaks of  $w$  superimposed on this deep layer of upward acceleration, but they correspond to smaller turbulent eddies rather than coherent thermals with collocated peaks in  $B$ . Note the sharp buoyancy peak near  $\sim 12 \text{ km}$  in Fig. 8h is not driven by latent heating from moist processes, but rather strong wave motion at the tropopause

likely driven by the overshooting updrafts. When  $L_H$  is reduced to 1 km in this moist environment, a much narrower cloud results and there are often multiple distinct thermals on the scale of the whole cloud at any given time. This is seen in vertical cross sections (Fig. 6, left column) as well as the distinct peaks of maximum  $w$  and  $B$  in Fig. 8 ( $w$  and  $B$  near 3.5 and 5.5 km at 115 min, separating by a valley of near zero  $w$  and  $B$ ). These peaks ascend over time, consistent with the thermal chain structure. Overall, the transition in updraft

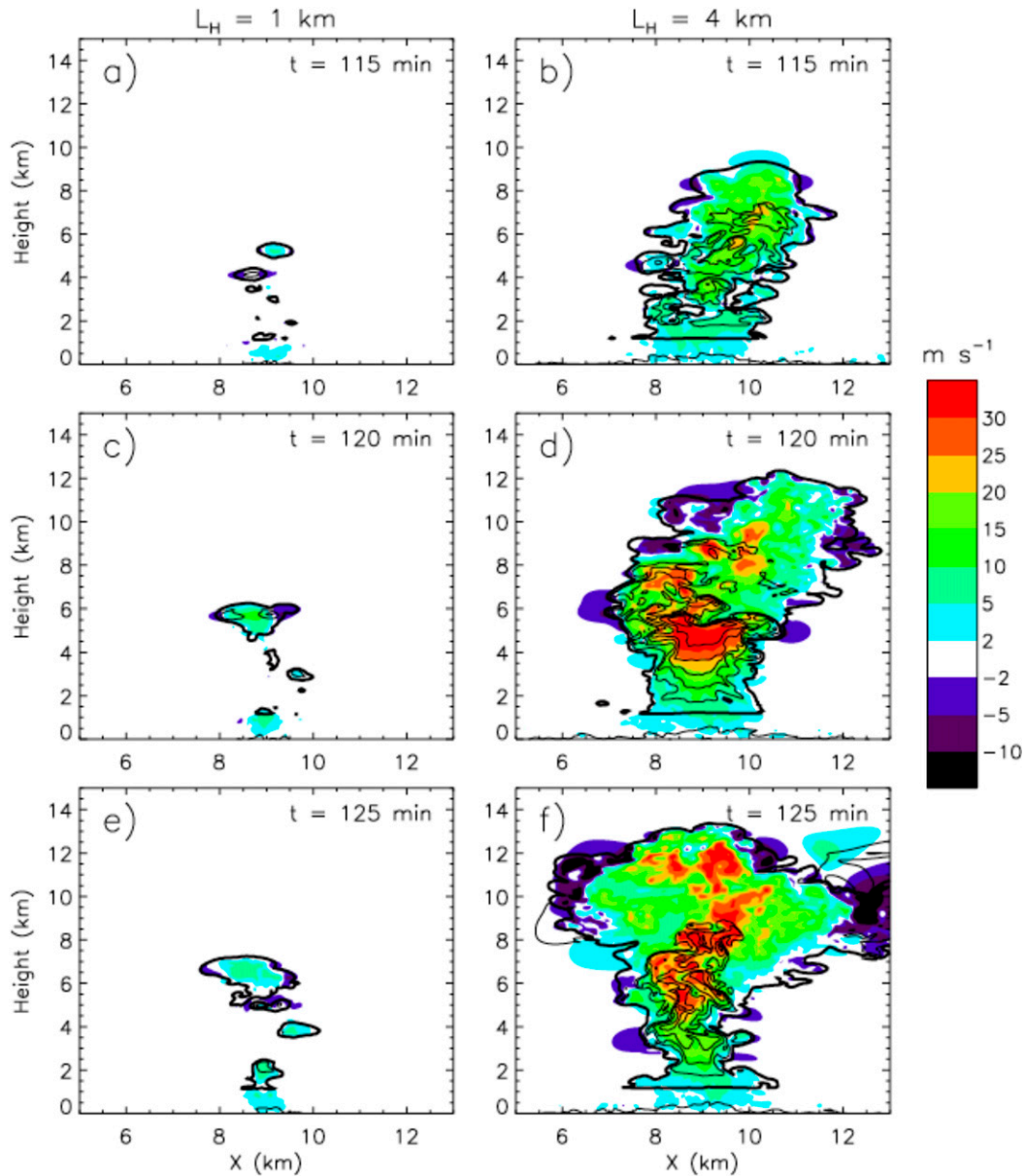


FIG. 6. As in Fig. 5, but for the moist environment with  $\phi_E = 0.9$  and (a),(c),(e)  $L_H = 1$  km or (b),(d),(f)  $L_H = 4$  km.

structure from isolated thermal, to thermal chain, to plume with increasing  $\phi_E$  and updraft width is consistent with the theoretical analysis of M20 and simulations of Peters et al. (2020). Those studies related these structural differences to the increasingly deleterious effects of dry air entrainment on buoyancy with decreases in cloud aspect ratio (width divided by height) and  $\phi_E$ .

Time series of several key quantities for the  $\phi_E = 0.3$  and 0.9 environments are shown in Figs. 9 and 10. These figures present results for four different values of  $L_H$  between 1000 and 4000 m and the three ensemble members. Convection

grows deep ( $z_B > 7.5$  km) in all of the moist  $\phi_E = 0.9$  runs regardless of the setting for  $L_H$ . Time series of  $w_{\max}$  show rapid intensification of convection in these runs, but with some weakening after 120–130 min for  $L_H$  of 2.5 and 4 km (Fig. 10c). Consistent with the discussion above, there is also a pulsating behavior of  $w_{\max}$  and  $B_{\max}$  associated with the life cycle of discrete rising thermals, most evident at moderate  $L_H$  (1.5 and 2.5 km). In contrast to the moist runs, the dry  $\phi_E = 0.3$  runs show a more gradual deepening when  $L_H$  is 2.5 and 4 km, with  $z_B$  exceeding 6 km only after 120 to 130 min. For smaller  $L_H$  (1 and 1.5 km) in this dry environment, convection

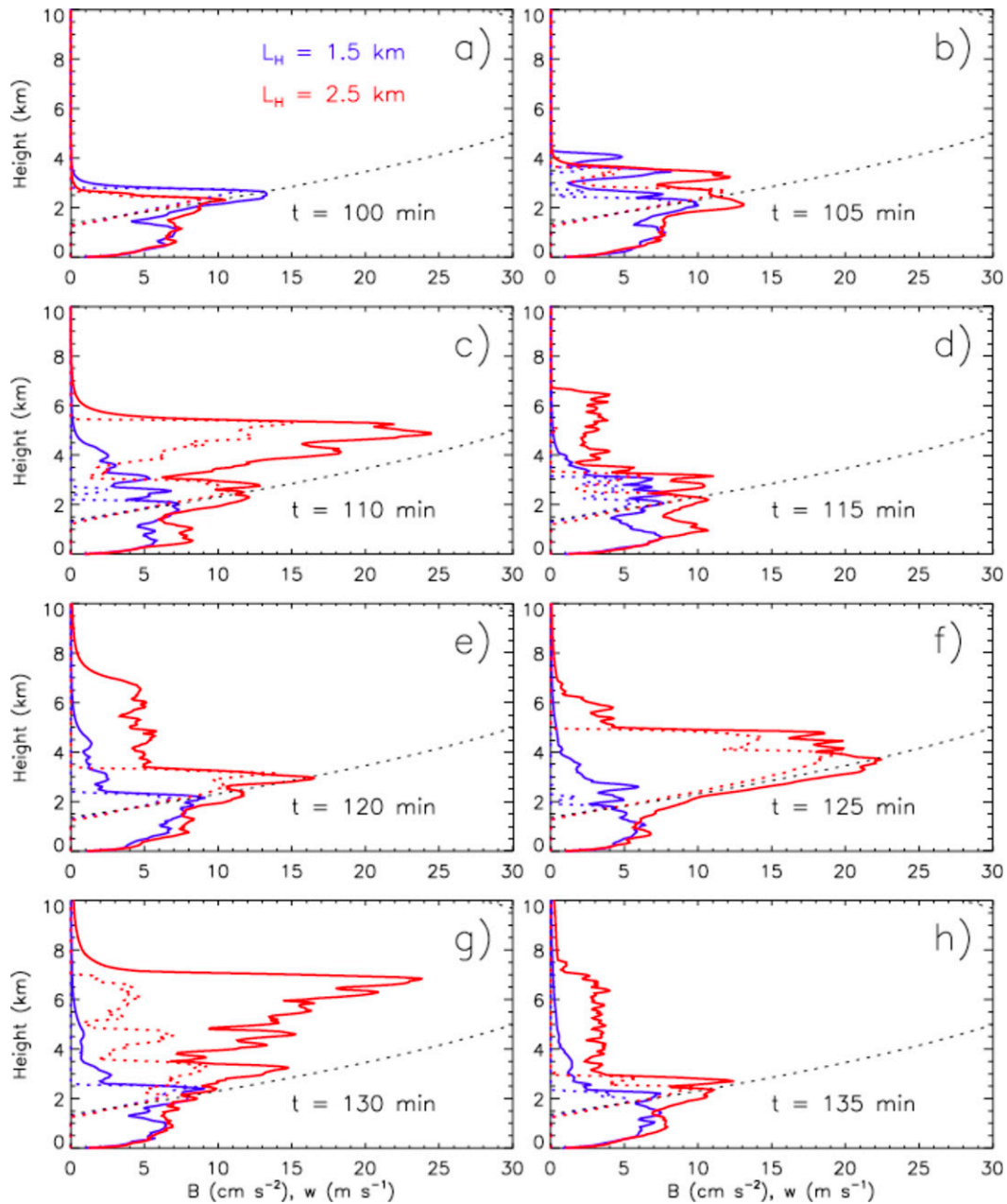


FIG. 7. Vertical profiles of horizontal-maximum vertical velocity  $w$  (solid lines) and in-cloud buoyancy  $B$  (dotted lines) considering points with  $w \geq 2 \text{ m s}^{-1}$  and cloud water mixing ratio  $\geq 0.1 \text{ g kg}^{-1}$ . Results for LESs with  $\phi_E = 0.3$  and  $L_H$  of 1.5 and 2.5 km are shown by blue and red lines, respectively. The thin dotted black line shows the pseudo-adiabatic buoyancy. Plots show profiles at different times as indicated, with an interval of 5 min.

remains shallow over the 3 h duration of the simulations with  $z_B$  below 4 km.

To understand how subcloud properties may impact convective properties above the LFC, particularly  $z_B$ , we also examine time series of the horizontal scale of subcloud ascent ( $R_{\text{sub}}$ ), maximum 250–1250 m layer  $w$  ( $w_{\text{sub,max}}$ ), and maximum 250–1250 m layer buoyancy ( $B_{\text{sub,max}}$ ) from the simulations with  $\phi_E$  of 0.3 and 0.9 (Figs. 9 and 10d–f). We define

$R_{\text{sub}} \equiv \sqrt{A/\pi}$  where  $A$  is the total area with  $w \geq 2 \text{ m s}^{-1}$  averaged between heights of 250 and 1250 m. As seen in Fig. 4 ( $w = 2 \text{ m s}^{-1}$  contour denoted by the thick black line), this  $w$  threshold captures the main area of ascent in the domain center while avoiding weaker ascent away from this region. For simplicity we define  $A$  using the total rather than contiguous area with  $w \geq 2 \text{ m s}^{-1}$ . This avoids having to choose an arbitrary threshold distance to define whether or not two

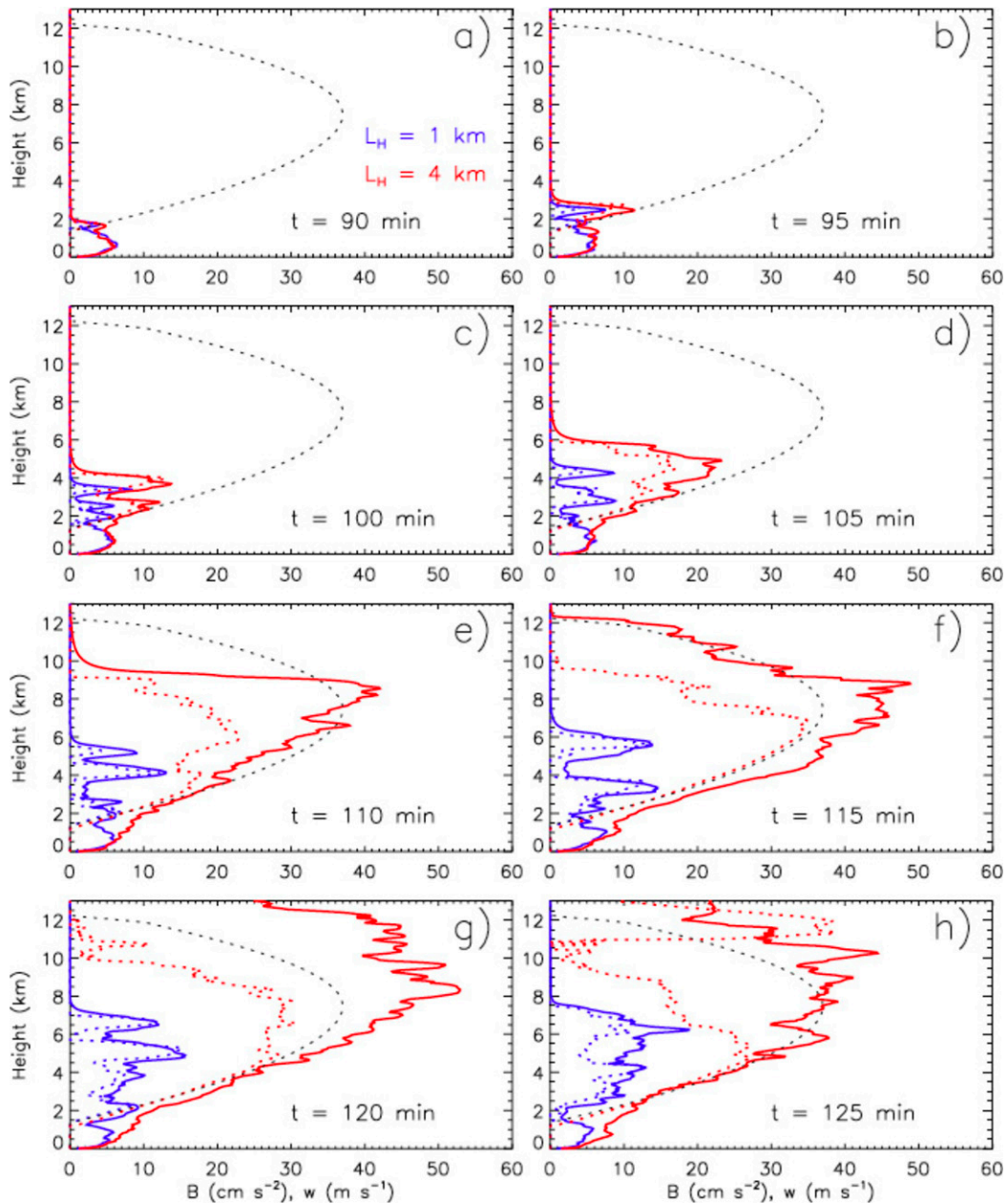


FIG. 8. As in Fig. 7, but for LESs with the moist  $\phi_E = 0.9$  environment and  $L_H$  of 1 km (blue lines) or 4 km (red lines).

nearby contiguous areas should constitute a single region of ascent; moreover, points with  $w \geq 2 \text{ m s}^{-1}$  are contiguous or nearly contiguous as seen in Fig. 4.

The value of  $R_{\text{sub}}$  is strongly related to  $L_H$ , which is expected since the surface flux forcing is a primary driver of the subcloud vertical motion. In turn  $z_B$  increases with  $R_{\text{sub}}$ , particularly for the  $\phi_E = 0.3$  LESs. In all runs  $R_{\text{sub}}$  increases over time up to  $\sim 100\text{--}120$  min and thereafter is fairly steady. It is also insensitive to  $\phi_E$ . Overall, the general picture is one of a positive relationship between  $L_H$ ,  $R_{\text{sub}}$ , and  $z_B$ , suggesting a linkage between the surface flux forcing, horizontal scale of subcloud ascent, and the height attained by buoyant moist

updrafts. In turn, updraft-core radius above cloud base is connected to  $R_{\text{sub}}$ . This is relevant because the theoretical expressions in section 2 are given in terms of updraft radius, and it establishes a physical linkage of features above cloud base and below. Figure 11 shows updraft-core radius  $R_c$  as a function of  $R_{\text{sub}}$  from all of the LESs. We define  $R_c \equiv \sqrt{A_c/\pi}$  where  $A_c$  is the total area at a given vertical level with  $w \geq 2 \text{ m s}^{-1}$ ,  $B \geq 0 \text{ m s}^{-2}$ , and  $q_c \geq 0.1 \text{ g kg}^{-1}$ . The value of  $R_c$  is calculated as a time average (140–180 min) and vertical average from cloud base to either 1 km above cloud base or the maximum cloud-top height, whichever is lower. A close relationship between  $R_c$  and  $R_{\text{sub}}$  is evident, though the more

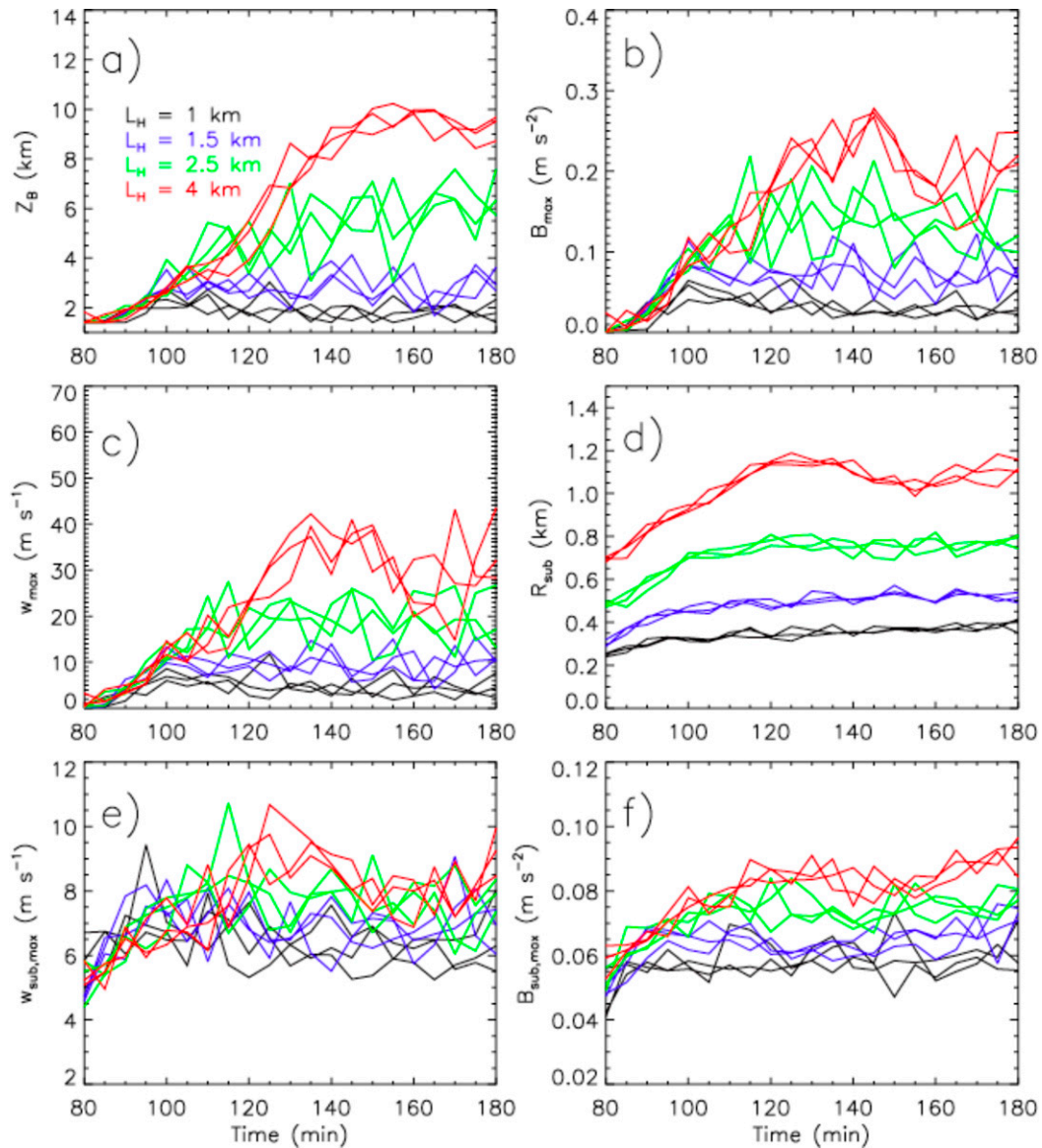


FIG. 9. Time series of (a) updraft equilibrium buoyancy height  $z_B$ , (b) maximum in-cloud buoyancy  $B_{\max}$  (LFC to 11-km height), (c) maximum in-cloud vertical velocity  $w_{\max}$ , (d) horizontal scale of subcloud ascent  $R_{\text{sub}}$ , (e) maximum subcloud vertical velocity  $w_{\text{sub,max}}$ , and (f) maximum subcloud buoyancy  $B_{\text{sub,max}}$  from the LESs with  $\phi_E$  of 0.3. Different colored lines the horizontal scale of the surface flux forcing  $L_H$  for the LESs as labeled in (a). Different lines of the same color show different ensemble members of a configuration. For clarity only LESs with  $L_H$  of 1, 1.5, 2.5, and 4 km are shown.

stringent cloud core definition leads to  $R_c$  being smaller than  $R_{\text{sub}}$  by  $\sim 0.2$  km. The  $R_c$  tends to be slightly larger ( $\sim 50$ – $100$  m) in the  $\phi_E = 0.9$  LESs, but otherwise variability among the LESs is small. Cloud  $R$ , calculated as above but considering only the cloud condensate threshold, is slightly larger than cloud core  $R$  (by roughly 20%) and scales closely with  $R_{\text{sub}}$ . For deeper updrafts there is much greater variability in core radius well above cloud base. This is seen in the vertical cross sections in Figs. 5 and 6, where the core size varies with time and height and is strongly influenced by the thermal-like

convective structures in some LESs. Considering the time-averaged (140–180 min) cloud core radii for deep updrafts ( $z_B \geq 8$  km) at the height of maximum  $w$  (Fig. 11, diamonds), the radii are larger than those near cloud base but there is also much more scatter among individual LESs. Despite this scatter, there is still a clear trend of larger upper-level cloud core radius with increasing  $R_{\text{sub}}$ . The cloud  $R$  (calculated using only the condensate threshold) at the height of maximum  $w$  for deep updrafts is larger than cloud core  $R$  at the same height by roughly a factor of 2, which is presumably a result

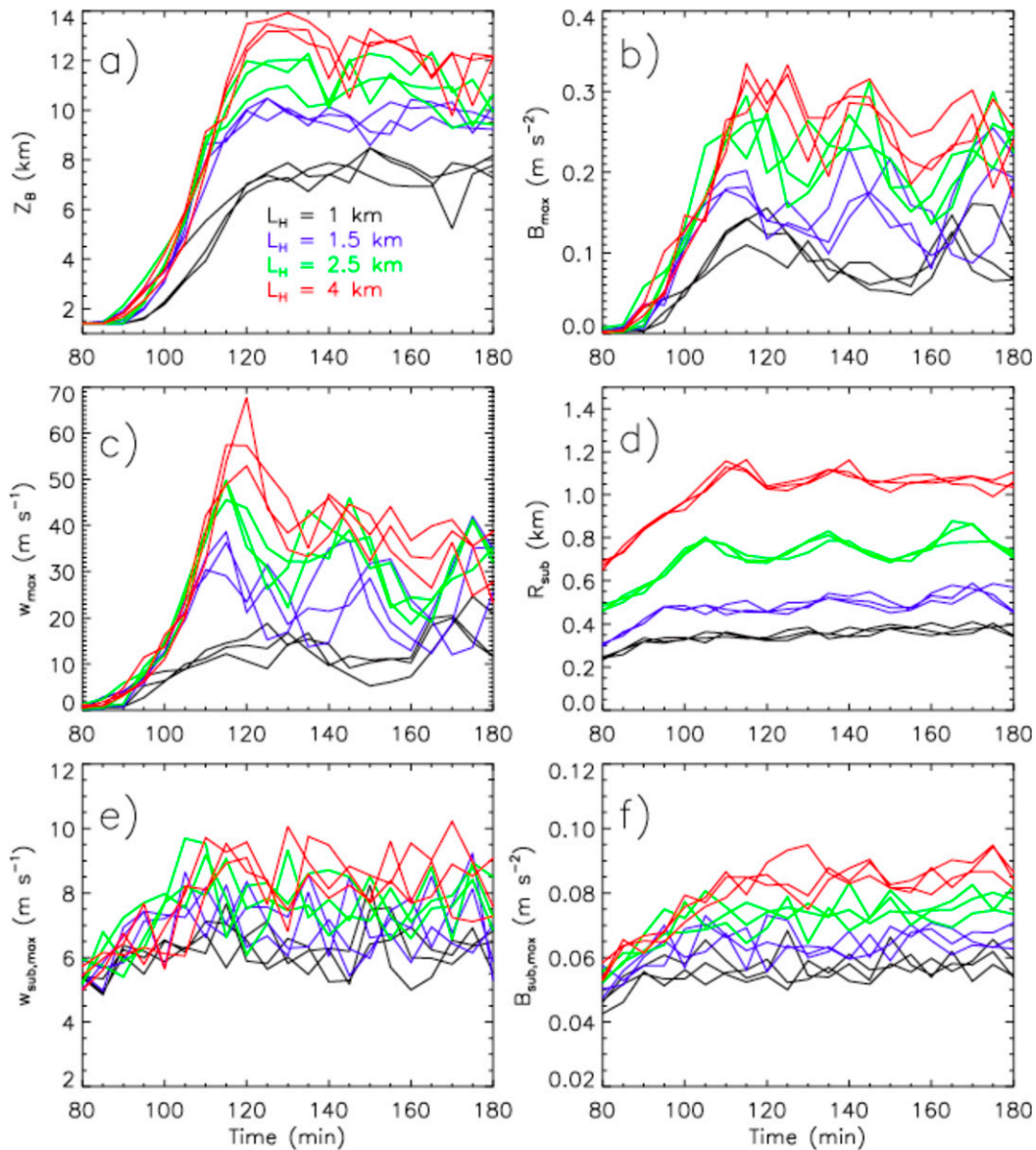


FIG. 10. As in Fig. 9, but for  $\phi_E$  of 0.9.

of condensate detrainment, especially above the height of maximum  $w$ .

Differences in subcloud  $w$  and  $B$  (quantified by  $w_{\text{sub,max}}$  and  $B_{\text{sub,max}}$ ) appear to be less influential than  $L_H$ ,  $R_{\text{sub}}$ , and  $R_c$  in driving differences in  $z_B$ . There is no consistent relationship between  $z_B$  and  $w_{\text{sub,max}}$  prior to convection going deep (before about 120 min). After deep convective initiation in some runs,  $w_{\text{sub,max}}$  generally increases with  $L_H$  and  $z_B$  although there is considerable scatter. This relationship is likely from the impact of cumulus dynamics on subcloud vertical motion, particularly increased upward perturbation pressure forcing below cloud in the presence of stronger, more buoyant updrafts (Leger et al. 2019).

Ascending parcels below cloud base are somewhat more buoyant when  $L_H$  is large, seen by the time series of  $B_{\text{sub,max}}$ . This is evident both before deep convective initiation and after, likely from reduced dilution of subcloud  $B$  when region of surface flux forcing is wide (keeping in mind that the maximum surface buoyancy flux is identical in all simulations). These differences in subcloud  $B$  could directly drive differences in convective cloud characteristics including  $z_B$ . However, the spread of  $B_{\text{sub,max}}$  as  $L_H$  is increased from 1 to 4 km is about  $0.02 \text{ m s}^{-2}$ , an order of magnitude smaller than differences in maximum  $B$  above cloud base. To explore the impact of subcloud buoyancy further, we ran an additional simulation ensemble with  $L_H = 1 \text{ km}$  and  $\phi_E = 0.3$  but the magnitude of

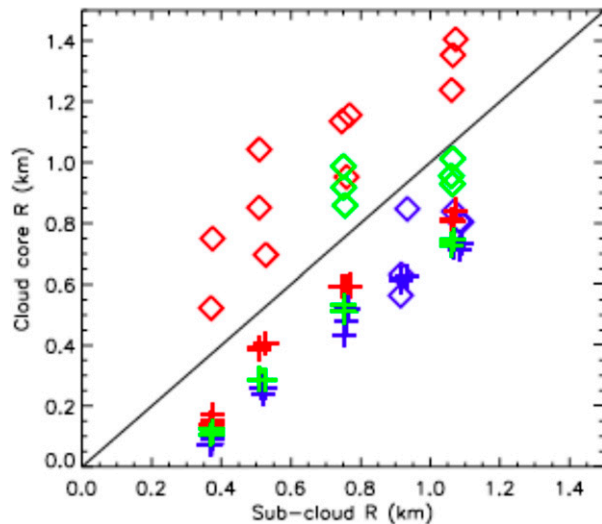


FIG. 11. Time-averaged (140–180 min) cloud updraft-core radius  $R_c$  (y axis) as a function of the radius of subcloud ascent  $R_{\text{sub}}$  (x axis) from the LESs ( $R_c$  and  $R_{\text{sub}}$  are defined in the main text). Crosses show values of  $R_c$  for each simulation averaged from cloud base to either cloud top or 1 km above cloud base (whichever is lower). Diamond symbols show values of  $R_c$  from each simulation averaged over a 1-km vertical layer centered on the height of maximum  $w$  for deep updrafts (defined as updrafts with  $z_B \geq 8$  km). Different colors indicate  $\phi_E$  of 0.3 (blue), 0.6 (green), and 0.9 (red). The black line indicates the 1:1 line.

the Gaussian-distributed surface flux forcing increased by a factor of 2. These runs produce almost the same time-mean (between 140 and 180 min)  $B_{\text{sub,max}}$  as the standard surface flux magnitude simulations with  $L_H = 4$  km (0.081 versus 0.084  $\text{m s}^{-2}$ ), but convection remains shallow with a time-mean  $z_B$  of 3.3 km. Moreover, doubling the surface flux magnitude increases  $R_{\text{sub}}$ , and the small increase in  $z_B$  with enhanced surface flux forcing is consistent with this increase in  $R_{\text{sub}}$ . Overall, we conclude that whether or not convection goes deep as  $L_H$  is increased is influenced much more by the increase in  $R_{\text{sub}}$  than subcloud  $B$  and  $w$ .

#### b. Comparison of $z_B$ and maximum $B$ from theory and LES

From the theory we obtain  $B$  profiles by integrating (4) as described in section 2; this provides theoretical values of  $z_B$  and maximum in-cloud  $B$ . For the thermodynamic sounding needed to specify  $Q$ ,  $T_E$ ,  $q_{sE}$ , and  $\Gamma$  in (4), we use the WK82 sounding consistent with the initial conditions for the LESs. There is some uncertainty in how best to specify  $R$  from a numerical simulation to compare to a theoretical calculation, particularly because of variability in height and time. For simplicity we use the time-averaged (140–180 min)  $R_{\text{sub}}$  from the LESs since  $R_{\text{sub}}$  is fairly steady in time and has little variability among ensemble members. As seen in Fig. 11, while there is scatter in cloud core radius  $R_c$  among the LESs, particularly above cloud base, there is a clear trend of increasing  $R_c$  with  $R_{\text{sub}}$  and a rough 1:1 correspondence between them. Values for all other parameters in the theoretical calculations are the same as described in section 2.

Figure 12a shows a comparison of time-averaged (140–180 min)  $z_B$  from the LESs and theory as a function of  $R_{\text{sub}}$  for  $\phi_E$  of 0.3, 0.6, and 0.9. Theoretical values are generally consistent with those from the LESs. In the drier environments there is a sharp increase of  $z_B$  as  $R_{\text{sub}}$  increases, and this transition occurs at larger  $R_{\text{sub}}$  as the  $\phi_E$  is increased. In the LESs, deep convection is sustained (with time-mean  $z_B > 8$  km) when  $R_{\text{sub}} \geq \sim 0.5, 0.75,$  and  $0.9$  km when  $\phi_E$  is 0.9, 0.6, and 0.3, respectively. These results support the “scale selection” hypothesis from section 2, though the shallow to deep transition (increase in  $z_B$  from 3 to 8 km) is sharper from the theoretical expressions than the LESs, especially for  $\phi_E = 0.3$ ; it occurs over a  $R_{\text{sub}}$  range of  $\sim 200$  m from the theory and  $\sim 400$  m in the LESs. Reasons for this difference are unclear but might be related to the weaker increase in updraft width above cloud base in drier environments as seen in Fig. 11, which is not accounted for by the theory.

Time-averaged (140 to 180 min) maximum in-cloud  $B$  values from the LESs are also compared with the theoretical maximum  $B$  as a function of  $R_{\text{sub}}$  (Fig. 12b). Maximum  $B$  increases with both  $R_{\text{sub}}$  and  $\phi_E$  similarly in the LESs and theory. Theoretical values are consistently smaller by about 0.03 to 0.06  $\text{m s}^{-2}$ , which may be due to neglecting subcloud buoyancy and assuming  $B = 0$  at the LFC in the theoretical calculations.

Because of the simplicity of the theoretical expression for  $B$ , we can easily ascertain cause and effect. To the extent that this expression provides a valid approximation of the LESs, it shows that changes in the horizontal updraft scale, which is an external parameter in the theory obtained from  $R_{\text{sub}}$ , drive changes in  $z_B$ . This occurs via changes in fractional entrainment rate  $\varepsilon$ , which increases as  $R_{\text{sub}}$  decreases. In turn, increased  $\varepsilon$  means greater dilution of buoyancy and decreased  $z_B$  as updraft radius decreases. While  $\phi_E$  does not directly impact  $\varepsilon$  in the theory, it determines how dry the entrained air is which strongly impacts the dilution of buoyancy through water phase changes.

#### c. Analysis of updraft dilution with a passive tracer

Results presented thus far indicate the role of enhanced updraft dilution from entrainment and mixing as the horizontal scale of subcloud ascent decreases. Not surprisingly, the dilution of buoyancy increases considerably as  $\phi_E$  decreases. Here we analyze dilution more directly with a passive tracer  $C$  initially set to 1  $\text{kg kg}^{-1}$  below 1.5 km and zero above. Figure 13 compares maximum height of the 0.5 and 0.8  $\text{kg kg}^{-1}$  contours of this tracer field from the theory in section 2 and LESs. Theoretical values are obtained by rearranging (3) to solve for  $z$  given a value of  $C$ . The time-averaged (140–180 min) values are plotted in Fig. 13 as a function of time-averaged  $R_{\text{sub}}$  from the LESs. Note the theoretical passive tracer has no direct dependence on  $\phi_E$  since  $\varepsilon$  is independent of  $\phi_E$ . Values of all other parameters used in the theoretical tracer calculations are given in section 2, and are the same as in the theoretical buoyancy calculations described in section 4b.

The theoretical expression (solid black lines in Fig. 13) gives a scaling with  $R_{\text{sub}}$  consistent with the LESs, although the  $C = 0.8 \text{ kg kg}^{-1}$  tracer value occurs somewhat higher (by

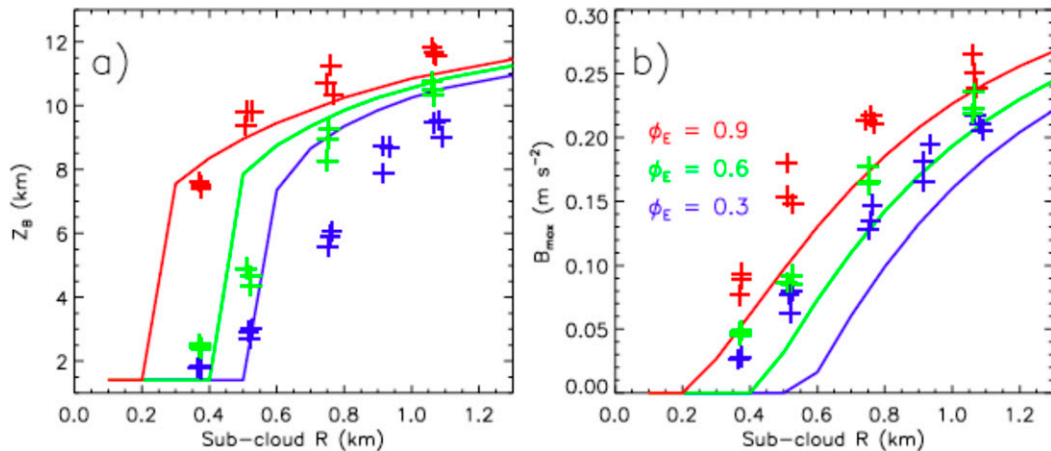


FIG. 12. Comparison of (a) updraft equilibrium buoyancy height  $z_B$  and (b) in-cloud (but below 11 km) maximum buoyancy  $B_{\text{max}}$  as a function of horizontal scale of subcloud ascent  $R_{\text{sub}}$  between the LESs (crosses) and theory calculated by vertical integration of (4) (lines). Colors represent different  $\phi_E$  values as labeled in (b).

$\sim 1$  km) in the LESs than theory when  $R_{\text{sub}} \geq 0.75$  km. While the heights of a given tracer value are sometimes greater in the moister environments than in the drier ones, differences are generally within the ensemble spread and thus are not robust. This supports the assumption in the theory that dilution of  $C$  is controlled by  $R_{\text{sub}}$  and not  $\phi_E$ —that is, that  $K_C$  and  $\varepsilon$  are independent of  $\phi_E$ .

Note that with a constant  $L = 120$  m the implied bulk fractional entrainment rate  $\varepsilon$  from (2) is proportional to  $R_{\text{sub}}^{-2}$  (see section 2). This value of  $L$  is used in all calculations presented in the paper (except as noted) since it gives the best fit compared to the LES results in Fig. 13. We also tested  $L = 0.13R_{\text{sub}}$  (dotted line in Fig. 13), where the proportionality constant of 0.13 gives the best fit when  $L$  is assumed to be proportional to  $R_{\text{sub}}$ . However, this gives slightly higher mean standard error (10%) than using  $L = 120$  m relative to the LESs.

Using  $L = 120$  m gives theoretical  $\varepsilon$  values of 0.80, 0.26, and  $0.13 \text{ km}^{-1}$  for  $R$  of 0.4, 0.7, and 1 km, respectively, following (2). These values are generally in line with previous bulk estimates, with values  $\sim 1 \text{ km}^{-1}$  or greater for shallow cumulus (e.g., Neggers et al. 2002; Siebesma et al. 2003) and  $\leq 0.5 \text{ km}^{-1}$  for deep cumulus (e.g., Kuang and Bretherton 2006; Del Genio and Wu 2010; De Rooy et al. 2013). However, we emphasize that our estimates of  $\varepsilon$  correspond to bulk dilution of the cloud regions that determine  $z_B$ , which are relatively undilute, and are therefore not necessarily representative of entrainment for the cloud as a whole. As described in previous studies from LES (Moser and Lasher-Trapp 2017; Peters et al. 2020) and theory (M2020),  $\varepsilon$  can vary substantially in different locations in a single cloud, with localized pulses of high entrainment rates associated with the toroidal circulations comprising the updraft flow.

#### d. Role of preconditioning by earlier cloud thermals

Here we distinguish between large-scale moistening by a field of shallow and congestus cumulus, and local effects from the rise of newer thermals directly into the wake of previous thermals (note the latter is neglected in the theoretical

analysis in section 2). The former occurs on time scales of  $\sim 1$  day (Waite and Khouider 2010) to several days (Hohenegger and Stevens 2013a), and thus is not directly relevant to our 3 h LESs. Nonetheless, the increase of  $z_B$  with increases in  $\phi_E$  in our simulations and theory is consistent with the role of large scale moisture preconditioning. In contrast to previous simulations exploring the role of moisture preconditioning on the shallow-to-deep transition (Waite and Khouider 2010; Yano and Plant 2012), our simulations have a larger-scale circulation forced by nonuniform surface fluxes. This continually focuses cumulus convection over the same region near the domain center. Thus, moistening from earlier cumulus occurs in a fairly small region at the domain center.

To explore the role of this moistening, we extended the  $\phi_E = 0.3$  and  $L_H = 1.5$ -km LESs to 6 h, with time series of various quantities shown in Fig. 14. In these LESs convection slowly deepens between 3 and 6 h, with  $z_B$  exceeding 7 km by 6 h (Fig. 14a). There is significant temporal variability in  $z_B$  and maximum  $w$  associated with the growth and decay of individual cloud thermals. The transition to deeper convection is accompanied by an increase in mean  $\phi_E$  of the cloud's near environment from about 0.3 to 0.41–0.44 by 6 h (Fig. 14d). This is defined by the mean relative humidity of all grid points within a cylindrical region around the cloud having a radius of 5 km and between 3- and 4-km height, excluding cloudy points with  $q_c \geq 0.001 \text{ g kg}^{-1}$ ). Note that this near-environment  $\phi_E$  depends on the size of the region over which it is calculated; thus, it should be understood as a qualitative rather than quantitative measure of the moistening of the cloud's near environment. There is also an increase in  $R_{\text{sub}}$  from  $\sim 0.5$  km to nearly 0.7 km between 3 and 6 h (Fig. 14c).  $R_{\text{sub}}$  values of  $\sim 0.7$  km are close to those in the  $L_H = 2.5$  km LESs from 2 to 3 h ( $\sim 0.7$ – $0.8$  km). Correspondingly,  $z_B$  and  $w_{\text{max}}$  values by 6 h are similar to those in the  $L_H = 2.5$ -km LESs at 2–3 h.

Combined with our theoretical analysis suggesting a relationship between  $R_{\text{sub}}$  and  $z_B$ , these results suggest that the

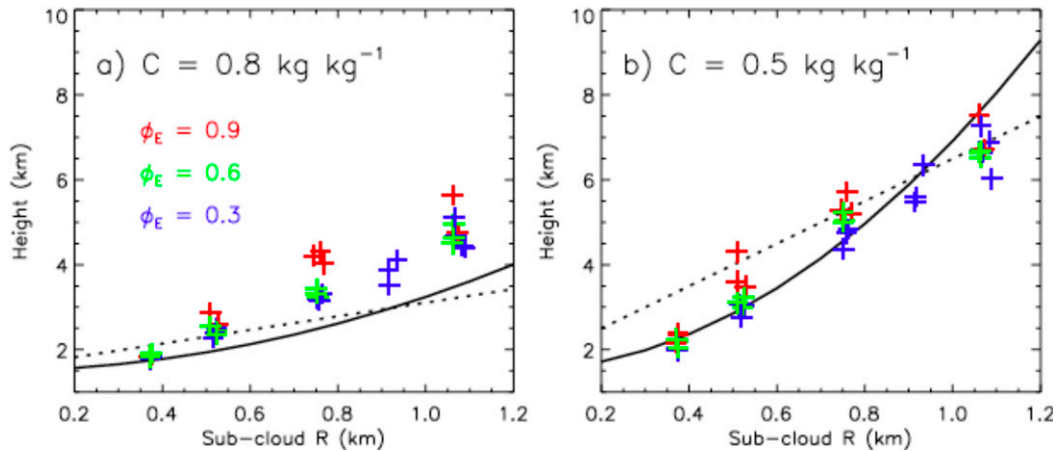


FIG. 13. Comparison of maximum height reached by values of the passive tracer field ( $C$ ): (a) 0.8 and (b) 0.5  $\text{kg kg}^{-1}$  from the LESs (crosses) and theory (black lines), as a function of horizontal scale of subcloud ascent  $R_{\text{sub}}$ . Solid black lines show theoretical values using  $L = 120$  m, and dotted black lines using  $L = 0.13R_{\text{sub}}$ . Crosses show values from each simulation (including different ensemble members) which are time averaged from 140 to 180 min.  $\phi_E$  of the LESs is indicated by colors as labeled in (a).

increase in  $z_B$  from 3 to 6 h can be mostly explained by the increase in  $R_{\text{sub}}$ . The increase in  $\phi_E$  of the near-cloud environment may also play a role in cloud deepening, but it is difficult to isolate the impact of this from the increase in  $R_{\text{sub}}$ . Overall, these results suggest that in the presence of organized circulations, even small changes in the horizontal scale of such circulations (i.e., few hundred meters) can have a large influence on cloud deepening. If the time scale of circulation changes is faster than moisture preconditioning, the latter is expected to have less influence in determining cloud-top heights.

The impact of newer thermals rising into the wake of earlier thermals is inferred by time series of convective quantities from the LESs in Figs. 9 and 10. In the moist environment ( $\phi_E = 0.9$ ) there is a sharp, near-monotonic increase in  $z_B$  between 95 and 120 min (Fig. 10a), indicating that earlier thermals have little impact on the height attained by subsequent thermals. Indeed, the structure of relatively wide updrafts (large  $L_H$ ) in the moist environment is more akin to a plume (or starting plume) rather than successive thermals as discussed in section 4a. In the dry environment ( $\phi_E = 0.3$ ), for the widest region of surface flux forcing ( $L_H = 4$  km) the behavior is similar to the moist case. In contrast, successive thermals are evident in the LESs with smaller  $L_H$  by sharp peaks and troughs in time series of  $z_B$  (Fig. 9a). However, in the LESs with  $L_H$  of 1- and 1.5-km successive thermals reach similar heights and remain shallow ( $z_B < 4$  km). Only in the low  $\phi_E$ ,  $L_H = 2.5$ -km LESs is there a progressive deepening of successive thermals, with local peaks in  $z_B$  near 4–5 km at 100–120 min but reaching 6–8 km after 140 min. These results suggest that the effects of newer thermals rising into the wake of previous thermals are greatest in marginal conditions for deep convective initiation (low  $\phi_E$ , moderate  $L_H$ ). The fairly limited impact of these effects overall may be due to dominance of mixing laterally (or from below) into thermals, rather than from their top; environmental air laterally mixed

into thermals is less likely to be strongly modified by earlier thermals than air mixed from the top. Moreover, the effects of modified wake air are complicated and the net impact is not obvious. Besides moistening, which would reduce the effect of buoyancy dilution from entrainment, there is cooling which has the opposite effect, and decay of earlier thermals can produce a broader region of negative buoyancy aloft that must be displaced by the next thermal (similar to wave drag). Finally, there are other pressure effects that might influence ascent of later thermals, such as reduced downward buoyant pressure forcing as successive thermals ascend and increase the height to width ratio of the cloud's buoyant region (Morrison 2016; Peters 2016).

## 5. Discussion and conclusions

In this study, we examined how environmental relative humidity  $\phi_E$  and horizontal scale of subcloud ascent  $R_{\text{sub}}$  impact deep convective initiation based on an analysis of LESs and theory. The theoretical analysis relied on simple expressions relating dilution of a passive tracer and buoyancy to  $\phi_E$  and updraft radius, the latter strongly influenced by  $R_{\text{sub}}$ . From this analysis, we proposed a “scale selection” hypothesis that suggested a minimum  $R_{\text{sub}}$  is required for convection to grow deep, and this minimum  $R_{\text{sub}}$  decreases with an increase in  $\phi_E$ . Specifically, the ratio of  $R_{\text{sub}}^2$  to saturation deficit  $(1 - \phi_E)$  must exceed a certain threshold value that depends on cloud-layer environmental lapse rate. Grabowski et al. (2006), Rochetin et al. (2014), and Rousseau-Rizzi et al. (2017) previously suggested a threshold horizontal cloud size is needed for convection to grow deep based on CRM and LES results. Here we formalized this concept and provided a theoretical context. A set of LESs using the CM1 model (50-m horizontal and vertical grid spacing) were performed to test this hypothesis. In these LESs  $\phi_E$  and  $R_{\text{sub}}$  were

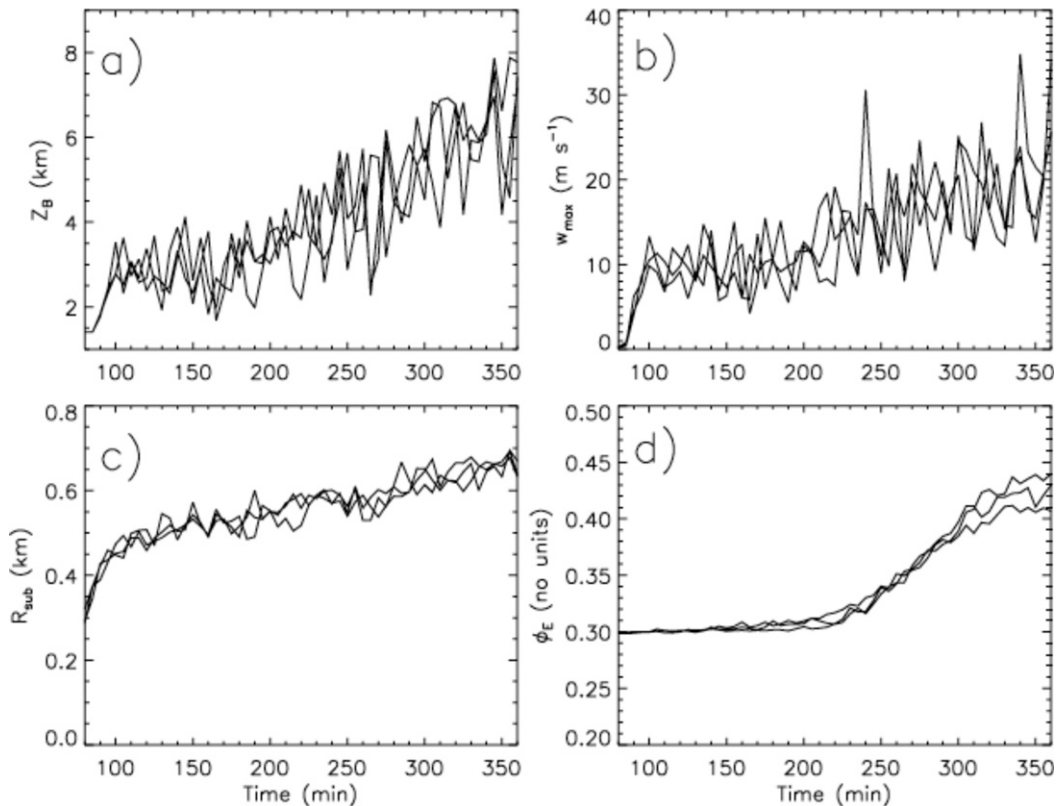


FIG. 14. Time series from the LESs with  $L_H = 1.5$  km and  $\phi_E = 0.3$  extended to 6 h. Results are presented for (a) updraft equilibrium height  $z_B$ , (b) maximum in-cloud vertical velocity  $w_{\max}$ , (c) horizontal scale of subcloud ascent  $R_{\text{sub}}$ , and (d) mean near-environment  $\phi_E$  calculated as described in the text. Lines show results from each of the three ensemble members.

systematically varied, with the latter altered by modifying the horizontal scale of surface flux forcing. Three ensemble members with different realizations were run for each LES configuration to improve robustness.

LES results were generally consistent with the theoretical expressions for the passive tracer and buoyancy, and thus supported the scale selection hypothesis. The LESs showed a transition from cumulus remaining shallow ( $<3$ -km height) to growing deep ( $>8$  km) with a change in  $R_{\text{sub}}$  of only  $\sim 400$  m, while the theoretical expressions showed this occurring over a smaller range of  $\sim 200$  m. This transition shifted to larger values of  $R_{\text{sub}}$  as  $\phi_E$  was decreased. Consistent with the theoretical expressions, the implied fractional entrainment rate  $\varepsilon$  from an analysis of passive tracer dilution decreased with an increase in  $R_{\text{sub}}$  but had little dependence on  $\phi_E$ . The strong sensitivity of updraft equilibrium height  $z_B$  in the LESs and theory to  $\phi_E$  was because of the impact of the relative humidity of entrained environmental air on buoyancy dilution. Rousseau-Rizzi et al. (2017) showed a similarly sharp transition in the average height attained by cloud thermals with an increase in thermal horizontal area at the LFC. Compared to  $R_{\text{sub}}$ , other subcloud properties (buoyancy and vertical velocity magnitudes) had much less influence on whether or not convection became deep in our simulations. This relative

insensitivity to thermodynamic properties near cloud base is consistent with Romps and Kuang (2010) and Böing et al. (2012). Those authors argued for the dominance of “nurture” (the conditions experienced by cloud updrafts above cloud base) in contrast to the role of “nature” (the thermodynamic conditions near cloud base) on convective cloud growth. However, our results suggest the critical role of “nature” if its definition is broadened to include the width of updrafts near cloud base, consistent with the view of Dawe and Austin (2012) and Rousseau-Rizzi et al. (2017). Similarly, Tian et al. (2021) showed that initial vertical momentum and buoyancy are critical for parcels overcoming CIN and reaching the LFC, but cloud size and  $\phi_E$  play a key role in determining cloud-top height via entrainment. They also noted the apparent role of vertical wind shear in limiting the vertical extent of convection.

Because of the strong sensitivity of  $z_B$  to  $R_{\text{sub}}$ , one of our main conclusions is that in a heterogeneous environment containing circulations of various spatiotemporal scales, small changes in the horizontal scale of coherent subcloud ascent can dictate a transition from shallow to deep convection. If such circulation changes occur over relatively short time scales (e.g.,  $<1$  day), this may limit the impact of other slower processes on the shallow-to-deep transition such as moisture preconditioning by evaporation of shallow or congestus

clouds. This idea is consistent with the picture put forth by Hohenegger and Stevens (2013a,b), who found that time scales of moisture preconditioning were generally longer than observations of the shallow-to-deep convective transition in both the tropics and midlatitudes. This is also consistent with previous studies showing that mesoscale circulations can concentrate ascent and produce much stronger convection even if  $\phi_E$ , and anticipated influences on cloud radius such as boundary layer thickness, are fixed (e.g., Robinson et al. 2008).

There are several caveats to mention. We turned off ice microphysics and precipitation generation, both of which complicate the picture. Ice microphysics can add a buoyancy “boost” from condensate freezing, particularly in environments with fairly weak lapse rates typical over tropical oceans. Precipitation can enhance downdrafts and generate cold pools, which strongly impact low-level circulations and subcloud vertical motion. Moreover, for simplicity we neglected the weight of condensate in the model’s buoyancy calculation. Including this reduces the buoyancy and lowers  $z_B$ , though an additional set of LESs that included condensate loading (not shown) exhibited qualitatively similar behavior, particularly the sensitivity to  $\phi_E$  and  $R_{\text{sub}}$ . To limit the number of parameters that were varied and keep the total number of simulations reasonable we used a single thermodynamic sounding (following WK1982) with fairly steep midtropospheric lapse rates. Our theoretical analysis showed that in the phase space of  $(\phi_E, R_{\text{sub}})$ , deep convective initiation is sensitive to pseudoadiabatic buoyancy and hence the cloud layer environmental lapse rate; in marginal conditions increased  $R_{\text{sub}}$  and/or  $\phi_E$  is needed for convection to grow deep when the pseudoadiabatic buoyancy is decreased. The initial thermodynamic profile for the LESs was also smooth, whereas real soundings typically have locally large vertical gradients of static stability and often one or more stable layers embedded within a wider layer that is unstable to pseudoadiabatic moist ascent. Such stable layers are expected to impact cumulus growth; in our framework, an increase in  $R_{\text{sub}}$  and/or  $\phi_E$  might be needed to overcome these layers. Finally, the surface flux forcing initiating moist convection in the model was fairly strong with subcloud vertical velocities up to several meters per second. In the future it would be worthwhile to explore controls on cumulus growth similarly to this study but with weaker forcing. Future work could also explore these controls in the situation of a deepening boundary layer forced by horizontally uniform surface fluxes (e.g., similar to the setup in Grabowski et al. 2006).

*Acknowledgments.* This work was supported by the U.S. Department of Energy Atmospheric System Research (DE-SC0000246356 and DE-SC0020104) and the Australian Research Council (ARC) Grant FL150100035. J. Peters’s efforts were also partially supported by the National Science Foundation Grant AGS-1841674. H. Morrison performed part of this work while on sabbatical and acknowledges support from ARC Centre of Excellence for Climate Extremes and the University of New South Wales Science Visiting Research Fellowship program. The National Center for Atmospheric Research is sponsored by the National Science

Foundation. We acknowledge high-performance computing support from Cheyenne (doi:10.5065/D6RX99HX) provided by NCAR’s Computational and Information Systems Laboratory. Comments on an earlier version of the paper by W. Grabowski are appreciated.

*Data availability statement.* The model code and initialization conditions for the numerical simulations and theoretical analysis for this study can be made available upon request to the first author.

## REFERENCES

- Anber, U. M., S. E. Giangrande, L. J. Donner, and M. P. Jensen, 2019: Updraft constraints on entrainment: Insights from Amazonian deep convection. *J. Atmos. Sci.*, **76**, 2429–2442, <https://doi.org/10.1175/JAS-D-18-0234.1>.
- Arakawa, A., and W. H. Schubert, 1974: Interaction of a cumulus cloud ensemble with the large-scale environment, Part I. *J. Atmos. Sci.*, **31**, 674–701, [https://doi.org/10.1175/1520-0469\(1974\)031<0674:IOACCE>2.0.CO;2](https://doi.org/10.1175/1520-0469(1974)031<0674:IOACCE>2.0.CO;2).
- Asai, T., and A. Kasahara, 1967: A theoretical study of compensating downward motions associated with cumulus clouds. *J. Atmos. Sci.*, **24**, 487–496, [https://doi.org/10.1175/1520-0469\(1967\)024<0487:ATSOTC>2.0.CO;2](https://doi.org/10.1175/1520-0469(1967)024<0487:ATSOTC>2.0.CO;2).
- Atkins, N. T., R. M. Wakimoto, and C. L. Ziegler, 1998: Observations of the finescale structure of a dryline during VORTEX 95. *Mon. Wea. Rev.*, **126**, 525–550, [https://doi.org/10.1175/1520-0493\(1998\)126<0525:OOTFSO>2.0.CO;2](https://doi.org/10.1175/1520-0493(1998)126<0525:OOTFSO>2.0.CO;2).
- Benedict, J. J., and D. A. Randall, 2007: Observed characteristics of the MJO relative to maximum rainfall. *J. Atmos. Sci.*, **64**, 2332–2354, <https://doi.org/10.1175/JAS3968.1>.
- Bladé, I., and D. L. Hartmann, 1993: Tropical intraseasonal oscillations in a simple nonlinear model. *J. Atmos. Sci.*, **50**, 2922–2939, [https://doi.org/10.1175/1520-0469\(1993\)050<2922:TIOIAS>2.0.CO;2](https://doi.org/10.1175/1520-0469(1993)050<2922:TIOIAS>2.0.CO;2).
- Bluestein, H. B., and S. S. Parker, 1993: Modes of isolated, severe convective storm formation along the dryline. *Mon. Wea. Rev.*, **121**, 1354–1372, [https://doi.org/10.1175/1520-0493\(1993\)121<1354:MOISCS>2.0.CO;2](https://doi.org/10.1175/1520-0493(1993)121<1354:MOISCS>2.0.CO;2).
- Blyth, A. M., and J. Latham, 1993: Development of ice and precipitation in New Mexican summertime cumulus clouds. *Quart. J. Roy. Meteor. Soc.*, **119**, 91–120, <https://doi.org/10.1002/qj.49711950905>.
- Böing, S. J., H. J. J. Jonker, A. P. Siebesma, and W. W. Grabowski, 2012: Influence of the subcloud layer on the development of a deep convective ensemble. *J. Atmos. Sci.*, **69**, 2682–2698, <https://doi.org/10.1175/JAS-D-11-0317.1>.
- Brown, R., and C. Zhang, 1997: Variability of midtropospheric moisture and its effect on cloud-top height distribution during TOGA COARE. *J. Atmos. Sci.*, **54**, 2760–2774, [https://doi.org/10.1175/1520-0469\(1997\)054<2760:VOMMAI>2.0.CO;2](https://doi.org/10.1175/1520-0469(1997)054<2760:VOMMAI>2.0.CO;2).
- Bryan, G. H., and J. M. Fritsch, 2002: A benchmark simulation for moist nonhydrostatic numerical models. *Mon. Wea. Rev.*, **130**, 2917–2928, [https://doi.org/10.1175/1520-0493\(2002\)130<2917:ABSFMN>2.0.CO;2](https://doi.org/10.1175/1520-0493(2002)130<2917:ABSFMN>2.0.CO;2).
- Chandrakar, K. K., W. W. Grabowski, H. Morrison, and G. H. Bryan, 2021: Impact of entrainment mixing and turbulent fluctuations on droplet size distributions in a cumulus cloud: An investigation using Lagrangian microphysics with a sub-grid-scale model. *J. Atmos. Sci.*, **78**, 2983–3005, <https://doi.org/10.1175/JAS-D-20-0281.1>.

- Chen, X., and F. Zhang, 2019: Relative roles of preconditioning moistening and global circumnavigating mode on the MJO convective initiation during DYNAMO. *Geophys. Res. Lett.*, **46**, 1079–1087, <https://doi.org/10.1029/2018GL080987>.
- Damiani, R., G. Vali, and S. Haimov, 2006: The structure of thermals in cumulus from airborne dual-Doppler radar observations. *J. Atmos. Sci.*, **63**, 1432–1450, <https://doi.org/10.1175/JAS3701.1>.
- Dawe, J. T., and P. H. Austin, 2011: Interpolation of LES cloud surfaces for use in direct calculations of entrainment and detrainment. *Mon. Wea. Rev.*, **139**, 444–456, <https://doi.org/10.1175/2010MWR3473.1>.
- , and —, 2012: Statistical analysis of an LES shallow cumulus cloud ensemble using a cloud tracking algorithm. *Atmos. Chem. Phys.*, **12**, 1101–1119, <https://doi.org/10.5194/acp-12-1101-2012>.
- Deardorff, J. W., 1980: Stratocumulus-capped mixed layers derived from a three-dimensional model. *Bound.-Layer Meteor.*, **18**, 495–527, <https://doi.org/10.1007/BF00119502>.
- Del Genio, A. D., and J. Wu, 2010: The role of entrainment in the diurnal cycle of continental convection. *J. Climate*, **23**, 2722–2738, <https://doi.org/10.1175/2009JCLI3340.1>.
- Derbyshire, S. H., I. Beau, P. Bechtold, J.-Y. Grandpeix, J.-M. Piriou, J.-L. Redelsperger, and P. M. M. Soares, 2004: Sensitivity of moist convection to environmental humidity. *Quart. J. Roy. Meteor. Soc.*, **130**, 3055–3079, <https://doi.org/10.1256/qj.03.130>.
- De Rooy, W. C., and A. P. Siebesma, 2010: Analytic expressions for entrainment and detrainment in cumulus convection. *Quart. J. Roy. Meteor. Soc.*, **136**, 1216–1227, <https://doi.org/10.1002/qj.640>.
- , and Coauthors, 2013: Entrainment and detrainment in cumulus convection: An overview. *Quart. J. Roy. Meteor. Soc.*, **139**, 1–19, <https://doi.org/10.1002/qj.1959>.
- García-Carreras, L., D. J. Parker, and J. H. Marsham, 2011: What is the mechanism for the modification of convective cloud distributions by land surface-induced flows? *J. Atmos. Sci.*, **68**, 619–634, <https://doi.org/10.1175/2010JAS3604.1>.
- Grabowski, W. W., 2020: Comparison of Eulerian bin and Lagrangian particle-based microphysics in simulations of non-precipitating cumulus. *J. Atmos. Sci.*, **77**, 3951–3970, <https://doi.org/10.1175/JAS-D-20-0100.1>.
- , and Coauthors, 2006: Daytime convective development over land: A model intercomparison based on LBA observations. *Quart. J. Roy. Meteor. Soc.*, **132**, 317–344, <https://doi.org/10.1256/qj.04.147>.
- Hernandez-Deckers, D., and S. C. Sherwood, 2016: A numerical investigation of cumulus thermals. *J. Atmos. Sci.*, **73**, 4117–4136, <https://doi.org/10.1175/JAS-D-15-0385.1>.
- , and —, 2018: On the role of entrainment in the fate of cumulus thermals. *J. Atmos. Sci.*, **75**, 3911–3924, <https://doi.org/10.1175/JAS-D-18-0077.1>.
- Heus, T., H. J. J. Jonker, H. E. A. van den Akker, E. J. Griffith, M. Koutek, and F. H. Post, 2009: A statistical approach to the life cycle of cumulus clouds selected in a virtual reality environment. *J. Geophys. Res.*, **114**, D06208, <https://doi.org/10.1029/2008JD010917>.
- Hohenegger, C., and B. Stevens, 2013a: Preconditioning deep convection with cumulus congestus. *J. Atmos. Sci.*, **70**, 448–464, <https://doi.org/10.1175/JAS-D-12-089.1>.
- , and —, 2013b: Reply to “Comments on ‘Preconditioning deep convection with cumulus congestus.’” *J. Atmos. Sci.*, **70**, 4155–4156, <https://doi.org/10.1175/JAS-D-13-0216.1>.
- Houston, A. L., and D. Niyogi, 2007: The sensitivity of convective initiation to the lapse rate of the active cloud bearing layer. *Mon. Wea. Rev.*, **135**, 3013–3032, <https://doi.org/10.1175/MWR3449.1>.
- Jeevanjee, N., 2017: Vertical velocity in the gray zone. *J. Adv. Model. Earth Syst.*, **9**, 2304–2316, <https://doi.org/10.1002/2017MS001059>.
- Johnson, R. C., T. M. Rickenbach, S. A. Rutledge, P. E. Ciesielski, and W. H. Schubert, 1999: Trimodal characteristics of tropical convection. *J. Climate*, **12**, 2397–2418, [https://doi.org/10.1175/1520-0442\(1999\)012<2397:TCOTC>2.0.CO;2](https://doi.org/10.1175/1520-0442(1999)012<2397:TCOTC>2.0.CO;2).
- Khairoutdinov, M., and D. Randall, 2006: High-resolution simulation of shallow-to-deep convection transition over land. *J. Atmos. Sci.*, **63**, 3421–3436, <https://doi.org/10.1175/JAS3810.1>.
- Kirshbaum, D. J., 2011: Cloud-resolving simulations of deep convection over a heated mountain. *J. Atmos. Sci.*, **68**, 361–378, <https://doi.org/10.1175/2010JAS3642.1>.
- Krueger, S., 1988: Numerical simulation of tropical cumulus clouds and their interaction with the subcloud layer. *J. Atmos. Sci.*, **45**, 2221–2250, [https://doi.org/10.1175/1520-0469\(1988\)045<2221:NSOTCC>2.0.CO;2](https://doi.org/10.1175/1520-0469(1988)045<2221:NSOTCC>2.0.CO;2).
- Kuang, Z., and C. S. Bretherton, 2006: A mass flux scheme view of a high-resolution simulation of a transition from shallow to deep cumulus convection. *J. Atmos. Sci.*, **63**, 1895–1909, <https://doi.org/10.1175/JAS3723.1>.
- Kuo, H. L., 1962: On the controlling influences of eddy diffusion on thermal convection. *J. Atmos. Sci.*, **19**, 236–243, [https://doi.org/10.1175/1520-0469\(1962\)019<0236:OTCIOE>2.0.CO;2](https://doi.org/10.1175/1520-0469(1962)019<0236:OTCIOE>2.0.CO;2).
- Kurowski, M. J., K. Suselj, W. W. Grabowski, and J. Teixeira, 2018: Shallow-to-deep transition of continental moist convection: Cold pools, surface fluxes, and mesoscale organization. *J. Atmos. Sci.*, **75**, 4071–4090, <https://doi.org/10.1175/JAS-D-18-0031.1>.
- Lasher-Trapp, S. G., W. A. Cooper, and A. M. Blyth, 2005: Broadening of droplet size distributions from entrainment and mixing in a cumulus cloud. *Quart. J. Roy. Meteor. Soc.*, **131**, 195–220, <https://doi.org/10.1256/qj.03.199>.
- Leger, J., J.-P. Lafore, J.-M. Piriou, and J.-F. Gueremy, 2019: A simple model of convective drafts accounting for the perturbation pressure term. *J. Atmos. Sci.*, **76**, 3129–3149, <https://doi.org/10.1175/JAS-D-18-0281.1>.
- Mapes, B., and R. Houze, 1995: Divergence profiles in western Pacific mesoscale convective systems. *J. Atmos. Sci.*, **52**, 1807–1828, [https://doi.org/10.1175/1520-0469\(1995\)052<1807:DDPIWP>2.0.CO;2](https://doi.org/10.1175/1520-0469(1995)052<1807:DDPIWP>2.0.CO;2).
- Masunaga, H., and C. D. Kummerow, 2006: Observations of tropical precipitating clouds ranging from shallow to deep convective systems. *Geophys. Res. Lett.*, **33**, L16805, <https://doi.org/10.1029/2006GL026547>.
- Morrison, H., 2016: Impacts of updraft size and dimensionality on the perturbation pressure and vertical velocity in cumulus convection. Part I: Simple, generalized analytic solutions. *J. Atmos. Sci.*, **73**, 1441–1454, <https://doi.org/10.1175/JAS-D-15-0040.1>.
- , 2017: An analytic description of the structure and evolution of growing deep cumulus updrafts. *J. Atmos. Sci.*, **74**, 809–834, <https://doi.org/10.1175/JAS-D-16-0234.1>.
- , G. Thompson, and V. Tatarskii, 2009: Impact of cloud microphysics on the development of trailing stratiform precipitation in a simulated squall line: Comparison of one and two-moment schemes. *Mon. Wea. Rev.*, **137**, 991–1007, <https://doi.org/10.1175/2008MWR2556.1>.

- , J. M. Peters, W. M. Hannah, A. C. Varble, and S. E. Giangrande, 2020: Thermal chains and entrainment in cumulus updrafts. Part I: Theoretical description. *J. Atmos. Sci.*, **77**, 3637–3660, <https://doi.org/10.1175/JAS-D-19-0243.1>.
- Morton, B. R., G. I. Taylor, and J. S. Turner, 1956: Turbulent gravitational convection from maintained and instantaneous sources. *Proc. Roy. Soc. London*, **A234**, 1–23, <https://doi.org/10.1098/rspa.1956.0011>.
- Moser, D. H., and S. Lasher-Trapp, 2017: The influence of successive thermals on entrainment and dilution in a simulated cumulus congestus. *J. Atmos. Sci.*, **74**, 375–392, <https://doi.org/10.1175/JAS-D-16-0144.1>.
- Mulholland, J. P., J. M. Peters, and H. Morrison, 2021: How does vertical wind shear influence entrainment in squall lines? *J. Atmos. Sci.*, **78**, 1931–1946, <https://doi.org/10.1175/JAS-D-20-0299.1>.
- Neggers, R. A. J., A. P. Siebesma, and H. J. J. Jonker, 2002: A multiparcel method for shallow cumulus convection. *J. Atmos. Sci.*, **59**, 1655–1668, [https://doi.org/10.1175/1520-0469\(2002\)059<1655:AMMFSC>2.0.CO;2](https://doi.org/10.1175/1520-0469(2002)059<1655:AMMFSC>2.0.CO;2).
- , P. G. Duynkerke, and S. M. A. Rodts, 2003a: Shallow cumulus convection: A validation of large-eddy simulation against aircraft and Landsat observations. *Quart. J. Roy. Meteor. Soc.*, **129**, 2671–2696, <https://doi.org/10.1256/qj.02.93>.
- , H. J. J. Jonker, and A. P. Siebesma, 2003b: Size statistics of cumulus cloud populations in large-eddy simulations. *J. Atmos. Sci.*, **60**, 1060–1074, [https://doi.org/10.1175/1520-0469\(2003\)60<1060:SSOCCP>2.0.CO;2](https://doi.org/10.1175/1520-0469(2003)60<1060:SSOCCP>2.0.CO;2).
- Nelson, T. C., J. Marquis, A. Varble, and K. Friedrich, 2021: Radiosonde observations of environments supporting deep moist convection initiation during RELAMPAGO-CACTI. *Mon. Wea. Rev.*, **149**, 289–309, <https://doi.org/10.1175/MWR-D-20-0148.1>.
- Parsons, D. B., M. A. Shapiro, R. M. Hardesty, R. J. Zamora, and J. M. Intrieri, 1991: The finescale structure of a west Texas dryline. *Mon. Wea. Rev.*, **119**, 1242–1258, [https://doi.org/10.1175/1520-0493\(1991\)119<1242:TFSOAW>2.0.CO;2](https://doi.org/10.1175/1520-0493(1991)119<1242:TFSOAW>2.0.CO;2).
- Peters, J. M., 2016: The impact of effective buoyancy and dynamic pressure forcing on vertical velocities within two-dimensional updrafts. *J. Atmos. Sci.*, **73**, 4531–4551, <https://doi.org/10.1175/JAS-D-16-0016.1>.
- , C. J. Nowotarski, and H. Morrison, 2019: The role of vertical wind shear in modulating maximum supercell updraft velocities. *J. Atmos. Sci.*, **76**, 3169–3189, <https://doi.org/10.1175/JAS-D-19-0096.1>.
- , H. Morrison, W. M. Hannah, A. C. Varble, and S. E. Giangrande, 2020: Thermal chains and entrainment in cumulus updrafts. Part II: Analysis of idealized simulations. *J. Atmos. Sci.*, **77**, 3661–3681, <https://doi.org/10.1175/JAS-D-19-0244.1>.
- Pielke, R. A., 2001: Influence of the spatial distribution of vegetation and soils on the prediction of cumulus convective rainfall. *Rev. Geophys.*, **39**, 151–177, <https://doi.org/10.1029/1999RG000072>.
- Raymond, D. J., and A. M. Blyth, 1989: Precipitation development in a New Mexico thunderstorm. *Quart. J. Roy. Meteor. Soc.*, **115**, 1397–1423, <https://doi.org/10.1002/qj.49711549011>.
- Rieck, M., C. Hohenegger, and C. C. van Heerwaarden, 2014: Influence of land surface heterogeneities on cloud size development. *Mon. Wea. Rev.*, **142**, 3830–3846, <https://doi.org/10.1175/MWR-D-13-00354.1>.
- Robinson, F. J., S. C. Sherwood, and Y. Li, 2008: Resonant response of deep convection to surface hot spots. *J. Atmos. Sci.*, **65**, 276–286, <https://doi.org/10.1175/2007JAS2398.1>.
- Rochetin, N., F. Couvreux, J.-Y. Grandpreux, and C. Rio, 2014: Deep convection triggering by boundary layer thermals. Part I: LES analysis and stochastic triggering formulation. *J. Atmos. Sci.*, **71**, 496–514, <https://doi.org/10.1175/JAS-D-12-0336.1>.
- Romps, D. M., 2010: A direct measure of entrainment. *J. Atmos. Sci.*, **67**, 1908–1927, <https://doi.org/10.1175/2010JAS3371.1>.
- , and Z. Kuang, 2010: Nature versus nurture in shallow convection. *J. Atmos. Sci.*, **67**, 1655–1666, <https://doi.org/10.1175/2009JAS3307.1>.
- Rousseau-Rizzi, R., D. J. Kirshbaum, and M. K. Yau, 2017: Initiation of deep convection over an idealized mesoscale convergence line. *J. Atmos. Sci.*, **74**, 835–853, <https://doi.org/10.1175/JAS-D-16-0221.1>.
- Schlemmer, L., and C. Hohenegger, 2014: The formation of wider and deeper clouds as a result of cold-pool dynamics. *J. Atmos. Sci.*, **71**, 2842–2858, <https://doi.org/10.1175/JAS-D-13-0170.1>.
- Sherwood, S. C., 1999: Convective precursors and predictability in the tropical western Pacific. *Mon. Wea. Rev.*, **127**, 2977–2991, [https://doi.org/10.1175/1520-0493\(1999\)127<2977:CPAPIT>2.0.CO;2](https://doi.org/10.1175/1520-0493(1999)127<2977:CPAPIT>2.0.CO;2).
- , and R. Wahrlich, 1999: Observed evolution of tropical deep convective events and their environment. *Mon. Wea. Rev.*, **127**, 1777–1795, [https://doi.org/10.1175/1520-0493\(1999\)127<1777:OEOTDC>2.0.CO;2](https://doi.org/10.1175/1520-0493(1999)127<1777:OEOTDC>2.0.CO;2).
- Shima, S.-I., and W. W. Grabowski, 2021: Isolated cumulus congestus based on SCMS campaign: Comparison between Eulerian bin and Lagrangian particle-based microphysics. *10th Int. Cloud Modeling Workshop 2021*, Pune, India, Indian Institute of Tropical Meteorology, <https://iccp2020.tropmet.res.in/Cloud-Modeling-Workshop-2020>.
- Siebesma, A. P., and Coauthors, 2003: A large eddy simulation intercomparison study of shallow cumulus convection. *J. Atmos. Sci.*, **60**, 1201–1219, [https://doi.org/10.1175/1520-0469\(2003\)60<1201:ALESIS>2.0.CO;2](https://doi.org/10.1175/1520-0469(2003)60<1201:ALESIS>2.0.CO;2).
- Squires, P., and J. S. Turner, 1962: An entraining jet model for cumulo-nimbus updrafts. *Tellus*, **14**, 422–434, <https://doi.org/10.1111/j.2153-3490.1962.tb01355.x>.
- Takayabu, Y. N., S. Shige, W.-K. Tao, and N. Hirota, 2010: Shallow and deep latent heating modes over tropical oceans observed with TRMM spectral latent heating data. *J. Climate*, **23**, 2030–2046, <https://doi.org/10.1175/2009JCLI3110.1>.
- Takemi, T., O. Hirayama, and C. Liu, 2004: Factors responsible for the vertical development of tropical oceanic cumulus convection. *Geophys. Res. Lett.*, **31**, L11109, <https://doi.org/10.1029/2004GL020225>.
- Tian, Y., Y. Zhang, S. A. Klein, and C. Schumacher, 2021: Interpreting the diurnal cycle of clouds and precipitation in the ARM GoAmazon observations: Shallow to deep convective transition. *J. Geophys. Res. Atmos.*, **126**, e2020JD033766, <https://doi.org/10.1029/2020JD033766>.
- Trier, S. B., F. Chen, and K. W. Manning, 2004: A study of convective initiation in a mesoscale model using high-resolution land surface initial conditions. *Mon. Wea. Rev.*, **132**, 2954–2976, <https://doi.org/10.1175/MWR2839.1>.
- Turner, J. S., 1957: Buoyant vortex rings. *Proc. Roy. Soc. London*, **A239**, 61–75, <https://doi.org/10.1098/rspa.1957.0022>.
- , 1962: The ‘starting plume’ in neutral surroundings. *J. Fluid Mech.*, **13**, 356–368, <https://doi.org/10.1017/S0022112062000762>.
- Waite, M. L., and B. Khouider, 2010: The deepening of tropical convection by congestus preconditioning. *J. Atmos. Sci.*, **67**, 2601–2615, <https://doi.org/10.1175/2010JAS3357.1>.

- Weisman, M. L., and J. B. Klemp, 1982: The dependence of numerically simulated convective storms on vertical wind shear and buoyancy. *Mon. Wea. Rev.*, **110**, 504–520, [https://doi.org/10.1175/1520-0493\(1982\)110<0504:TDonSC>2.0.CO;2](https://doi.org/10.1175/1520-0493(1982)110<0504:TDonSC>2.0.CO;2).
- Xu, K., A. Arakawa, and S. Krueger, 1992: The macroscopic behavior of cumulus ensembles simulated by a cumulus ensemble model. *J. Atmos. Sci.*, **49**, 2402–2420, [https://doi.org/10.1175/1520-0469\(1992\)049<2402:TMBOCE>2.0.CO;2](https://doi.org/10.1175/1520-0469(1992)049<2402:TMBOCE>2.0.CO;2).
- Yano, J.-I., and R. Plant, 2012: Interactions between shallow and deep convection under a finite departure from convective quasi equilibrium. *J. Atmos. Sci.*, **69**, 3463–3470, <https://doi.org/10.1175/JAS-D-12-0108.1>.
- Yeung, N. H., S. C. Sherwood, A. Protat, T. P. Lane, and C. Williams, 2021: A Doppler radar study of convective draft lengths over darwin, australia. *J. Atmos. Sci.*, **149**, 2965–2974, <https://doi.org/10.1175/MWR-D-20-0390.1>.
- Yuter, S., R. Houze, E. Smith, T. Wilheit, and E. Zipser, 2005: Physical characteristics of tropical oceanic convection observed in KWAJEX. *J. Appl. Meteor.*, **44**, 385–415, <https://doi.org/10.1175/JAM2206.1>.
- Zermeño-Díaz, D. M., C. Zhang, P. Kollias, and H. Kalesse, 2015: The role of shallow cloud moistening in MJO and non-MJO convective events over the ARM Manus site. *J. Atmos. Sci.*, **72**, 4797–4820, <https://doi.org/10.1175/JAS-D-14-0322.1>.
- Zhang, Y., and S. A. Klein, 2010: Mechanisms affecting the transition from shallow to deep convection over land: Inferences from observations of the diurnal cycle collected at the ARM Southern Great Plains site. *J. Atmos. Sci.*, **67**, 2943–2959, <https://doi.org/10.1175/2010JAS3366.1>.
- Ziegler, C. L., T. J. Lee, and R. A. Pielke, 1997: Convective initiation at the dryline: A modeling study. *Mon. Wea. Rev.*, **125**, 1001–1026, [https://doi.org/10.1175/1520-0493\(1997\)125<1001:CIATDA>2.0.CO;2](https://doi.org/10.1175/1520-0493(1997)125<1001:CIATDA>2.0.CO;2).